Cryogenic Strain Application to Two-Dimensional Electron Systems and the Stripe State

Senior Thesis by

Bart H. McGuyer

Mentor

James P. Eisenstein

In Partial Fulfillment of the Requirements

for the Degree of

Bachelor of Science

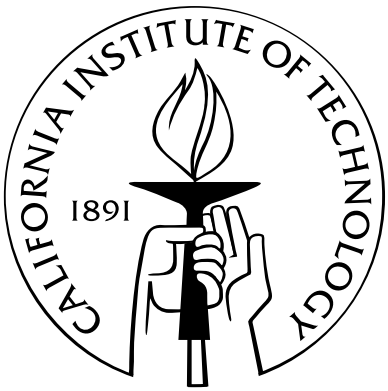

California Institute of Technology

Pasadena, California

2006

(Submitted March 8, 2006)

Acknowledgements

This project would not have been possible without the Eisenstein research group, the Caltech Summer Undergraduate Research Fellowship (SURF) program, and the Donald S. Clark Fellowship.

I am especially indebted to Jim Eisenstein for his guidance over the past two years. Jim, thank you for keeping your door open and the discussion lively as we plodded through all my quirky data and miscellaneous questions. I cannot thank you enough for giving me the opportunity to work in your lab, and for introducing me to condensed matter and the fascinating realm of two-dimensional electron physics. In that respect, I must also thank Michael Cross for introducing me to Jim in the first place, in addition to being a good advisor over the past four years.

The experience I have gained through my work with the Eisenstein group has been invaluable to my physics education, and in large part this is true as a result of my good fortune to work with the members of the group. To Lisa Tracy, thank you for always lending a helping hand, and–to borrow a phrase–keeping the Sloan subbasement filled with good humor and physics. To Alex Champagne and Ghislain Granger, thank you for helping me with sample processing for this project, and for all of your general advice and tales of experience. To the resident machinist Steve Stryker, thank you for answering all my mechanical questions, no matter what the topic. Additionally I would like to thank all of the other members of the group that I have had the pleasure to work with over the past two years: Tony Bonetti, Ian Spielman, Xerxes Lopez-Yglesias, Aaron Fink, Ben Olson, and Dale Syphers.

Last but not least, I must thank my fiancé Melissa Miller for her loving support, and her unwavering confidence in me.

Abstract

Electrons confined to move in a plane are collectively known as a two-dimensional electron system (2DES). Engineered GaAs/AlGaAs samples are grown to create 2DESs between internal layers. At very low temperatures and in the presence of a large perpendicular magnetic field, 2DESs have lead to the discovery of striking new physics such as the various quantum Hall effects and a recently discovered anisotropic state. Characterized by a large difference between conduction along two orthogonal in-plane crystal axes, the anisotropic state is referred to as the stripe state due to the suspicion of electron density stripe pattern formation. We present progress towards probing the physics of the stripe state through in situ application of strain on GaAs/AlGaAs samples using commercial piezo-actuators. This experiment will provide further insight into the orientational mechanism that serves to align the stripe state anisotropy axes.

Contents

Acknowledgements **iii**

Abstract **v**

1 Summary **1**

2 Introduction **3**

2.1 Two-Dimensional Electron Systems 3

2.2 Landau Levels 3

2.3 Magnetotransport 4

2.4 The Stripe State 6

2.5 Project Motivation: Stripe State Orientation Mechanism 7

2.6 Strain and Two-Dimensional Electron Systems 9

3 Experimental Methods **11**

3.1 Two-Dimensional Electron System Samples 11

3.1.1 Processing 11

3.1.2 2DES Electrical Measurement 12

3.2 Cryogenics 13

3.3 Piezo-Header Method 14

3.3.1 Design 14

3.3.2 Piezo-Actuator Control 15

3.3.3 Strain Measurement 16

3.3.4 PH 2DES Measurement Procedure 17

4 Piezo-Header Results **19**

4.1 2005 SURF 19

4.2 Physics 78 21

4.2.1 PH-11 24

4.3 Piezo-Header Performance 25

5 2DES Results **27**

5.1 Data Origins . . . 27

5.2 $B_\perp = 0$ . . . 29

5.3 Magnetotransport . . . 29

5.4 Discussion . . . 30

6 Conclusion **33**

Appendices

A Strain **35**

A.1 Introduction . . . 35

A.2 Uniaxial Strain . . . 36

A.3 Solid Deformation and Poisson Strain . . . 36

A.4 Directional Strain in Two-Dimensions . . . 37

A.5 Strain Distribution in 2DES Samples . . . 38

B Strain Measurement **39**

B.1 Strain Gauges . . . 39

B.2 Wheatstone Bridge . . . 40

B.2.1 Wheatstone Bridge with Strain Gauges . . . 41

C Piezo-Header Addendum **43**

C.1 Parts . . . 43

C.2 Detailed Construction . . . 43

D Sample Processing **45**

D.1 Cleaving . . . 45

D.2 Thinning . . . 46

D.3 Photolithography . . . 46

D.3.1 Sample Cleaning . . . 46

D.3.2 Mesa-Etch . . . 46

D.3.3 Ohmic Contacts Mask . . . 47

D.3.4 Evaporating Ohmic Contacts . . . 47

E About This Document **49**

Bibliography **51**

Chapter 1

Summary

The goal of this project was to perfect a method of applying controllable uniaxial strain on two-dimensional electron systems (2DESs) at cryogenic temperatures and in the presence of large magnetic field strengths, with the ultimate aim of utilizing this technique to investigate the alignment mechanism of the anisotropic stripe state. At this moment, we have successfully developed such a method, and we have performed initial measurement of the effects of strain on 2DESs not in the stripe state. We have not, however, performed a test on the stripe state, although a new device under construction may address this shortcoming before the end of the year.

The work completed results from a continual refinement of process and technique on all levels. Our approach stems from the ingenious demonstration by M. Shayegan et al. [1] that commercial piezo-actuators may be used at cryogenic temperatures to apply strain on thinned semiconductor samples. We incorporated this idea into what we refer to as "piezo-headers" (PH), which are small devices that can fit into the tiny space available at the sample stages of our cryogenic equipment. By attaching a 2DES sample to a piezo-header, we can apply strain *in situ* to the sample at cryogenic temperatures. We measure this strain through metallic foil strain gauges and a homemade low-power Wheatstone bridge to an accuracy of about a ppm.

In total, we have built ten piezo-headers in succession, referred to as PH-1 to PH-10, seven of which incorporate 2DES samples. Each piezo-header is a refinement of the previous models. We built and tested the first six PHs last summer, as a Summer Undergraduate Research Fellowship (SURF), and the last four PHs during this school year, for Physics 78. A special eleventh piezo-header, PH-11, is currently half completed; sample processing and attachment still remain. This version will use a 2DES sample from a different wafer than the rest of the piezo-headers, a wafer which is known to produce a good stripe state.

The most unexpected discoveries in this project revolve around the selection and operation of the piezo-actuators. During the summer, we learned that we must use cryogenic application piezo-actuators, instead of the standard piezo-actuator mentioned in [1]. In addition, we learned very recently the importance of cooling the piezo-actuators with their leads open, instead of with their

leads shorted as the manufacturer recommends to handle potentially hazardous voltages created during thermal cycling. Cooling with the leads shorted results in large frozen-in strains that disrupt the 2DES; cooling with the leads open does not do this. Only the most recent tests of PH-9 were performed with the piezo-actuator leads open during thermal cycling. All previous tests had the leads shorted, and suffered from frozen-in strain.

Our PH approach is complicated, and relies almost entirely on hand-assembly during construction. As such, the error rate is high. For example, strain gauges fail (ex: PH-7), the samples can be damaged (ex: PH-8), and ground shields may have complications (ex: PH-9 and PH-10). In particular, the failure of the ground shield of PH-9 went unnoticed until very recently. A quick repair has fixed the shield, and since then we have re-taken data. A new method of ground shield construction is planned for PH-11 to avoid the problems encountered by PH-9 and PH-10. The recent PH-9 data, taken with a repaired ground shield and with the piezo-actuator leads open during cooling, forms the core of this project, as it is the only true data we have of the effects of uniaxial strain alone on 2DESs.

Despite all of the difficulties, we have demonstrated that the current PH method works. We have repeatedly applied strains of up to about $\pm 5 \times 10^{-5}$ on samples at T = 4.2 K and 0.3 K and with magnetic field strengths of up to 0.63 Tesla, with negligible creep and hysteresis. We have demonstrated that PHs thermally re-cycle, with PH-9 setting the record so far with five complete cycles from room temperature to T = 0.3 K and back. The effects of uniaxial strain alone can be studied with our current design.

In retrospect, we recognize that the original goal of the project, to develop and execute a method to test the effects of strain on the anisotropy orientation of the stripe state, was very ambitious. However, we have successfully developed a difficult method for the cryogenic application of uniaxial strain, and we have initially documented the effects of uniaxial strain on 2DESs. Work is under way, through PH-11, to apply this method to a stripe state sample, so the chance remains that we may have the beginning of an answer to our initial question before the year is over.

Chapter 2

Introduction

This chapter gives a brief overview of the physics of two-dimensional electron systems (2DESs). For more information, please see the following two excellent references [2, 3].

2.1 Two-Dimensional Electron Systems

A system of electrons confined into a two-dimensional sheet is collectively known as a two-dimensional electron system. Amazingly, such a seemingly simple system is host to a remarkable array of interesting physics, especially when low temperatures and transverse magnetic fields are used to create a correlated electron system, where inter-electron interactions are significant. The study of 2DESs over the past three decades has lead to the discovery of many exotic phenomena, including the various quantum Hall effects. Perhaps most striking is the fractional quantum Hall effect (FQHE), where charge transport is observed with $^1/_3$ the fundamental unit.

The observation of a new anisotropic state in 1999 provides yet another example of the surprising physics present in 2DESs [4]. Characterized by a large difference between conduction along two in-plane orthogonal axes, this state is also known as the stripe state due to the suspicion of alternating high and low electron density stripe pattern formation. While much is known about the stripe state, the exact identity of the mechanism responsible for orienting the anisotropy axes remains unclear [5]. However, before we can continue to discuss the stripe state, we must cover some necessary details about 2DESs.

2.2 Landau Levels

The introduction of a uniform transverse magnetic field $B_\perp$ on a 2DES resolves the density of states $n(E)$ into a series of delta functions with energies $(N+\frac{1}{2})\hbar\omega_c$, known as Landau levels (LLs), where $N = 0,\ 1,\ 2,\ \ldots$, and ω_c is the classical cyclotron frequency $\omega_c = |\frac{eB}{m}|$. Each Landau level is in turn spin split by the Zeeman energy, $\pm\frac{1}{2}g\mu_B B_\perp$, where the gyromagnetic ratio g depends on the

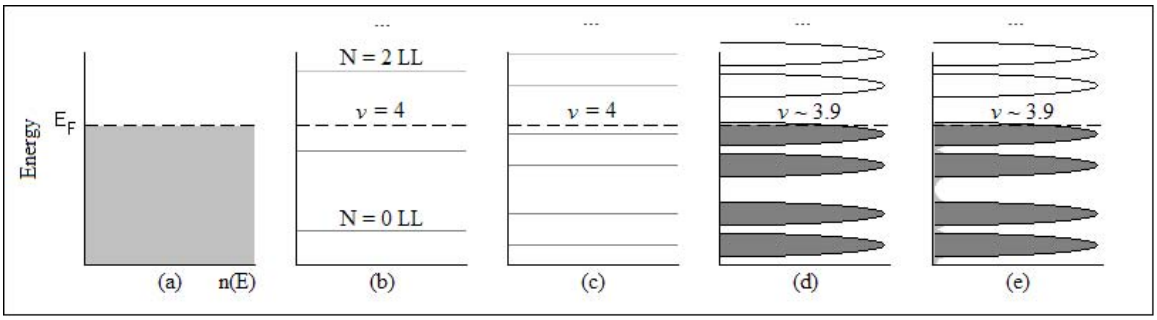

Figure 2.1: *2D Density of States. (a) Example continuous spectrum. (b) Partitioning into Landau levels by a magnetic field. (c) Spin splitting included. (d) Landau levels broadened from disorder. (e) Localized states included.*

host material (g = -0.44 for GaAs).

The number of occupied Landau levels is conveniently expressed with the filling factor $\nu = \frac{N_s}{n_B}$, where $n_B = \frac{e}{h}B_\perp$ and N_s is the 2D electron carrier density (not to be confused with the LL index N). The filling factor counts each spin split LL individually, as depicted in figure 2.1. For example, when all of the $N \leq n$ LLs are occupied, $\nu = 2n + 2$. When the Nth LL is partially occupied, ν lies between $2N$ and $2(N + 1)$. If only one spin split half of the Nth LL is occupied, then $\nu = 2N + 1$, and if that spin split half LL is partially occupied, then ν is a fraction between $2N$ and $2N + 1$. Please refer to figure 2.1 if this is unclear.

In practice, the energies of the electrons in a Landau level are broadened by scattering from phonons, other electrons, and lattice disorder (Figure 2.1 (d)). Imperfections also serve to create localized states with random energies, which add a background to the density of states between the LLs (Figure 2.1 (e)).

The 2DESs important to this research are created inside semiconductor heterostructures, which always have impurities and defects. Electron mobility, μ (10^6 cm^2/Vs), is a convenient indicator of the quality of a particular 2DES sample. The higher the mobility of a sample, the closer the sample is to ideal. The samples used for this project all derive from the same wafer, which has a typical $\mu \simeq 9$. Samples of roughly this mobility and greater are referred to as "high mobility" samples, by today's standards. The highest current mobility reached in a similar 2DES sample is $\mu = 31$. In a sense, high mobility is a necessity for the pursuit of new physics in 2DESs, as often extremely fragile novel states are discovered as a result of increased sample mobility.

2.3 Magnetotransport

In two-dimensions and in the presence of a transverse magnetic field, conductivity and resistivity are not inversely related scalars. Instead, both are tensors (2x2 matrices). As a result, there are two types of electrical resistance measurements performed on 2DESs: directional and Hall measure-

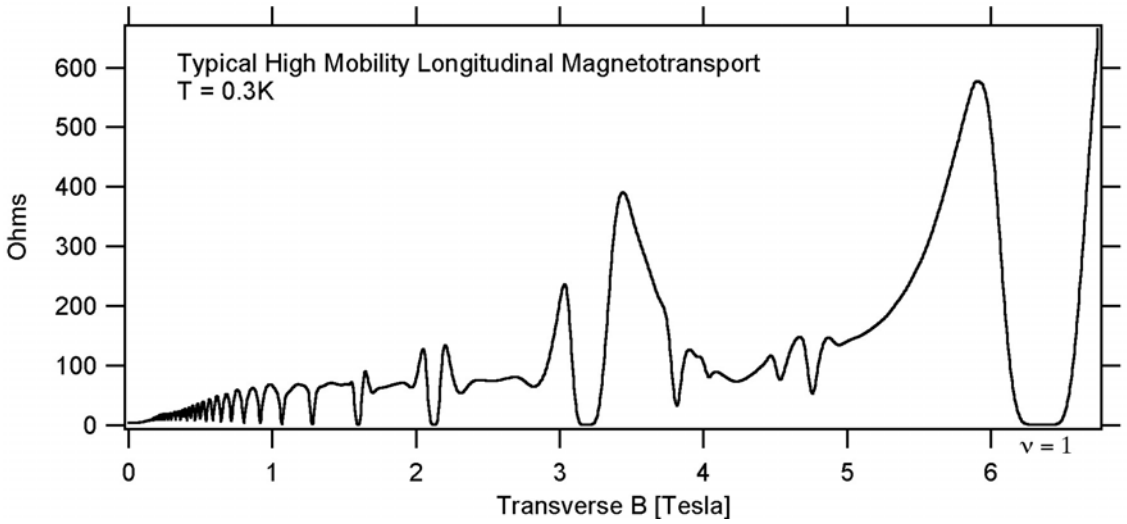

Figure 2.2: *Shubnikov-de Haas oscillations in the directional resistance of the 2DES sample used for PH-7, before gluing.*

ments. In a directional resistance measurement, such as R_{xx} and R_{yy}, voltage is measured across the sample in the same direction as the current flow. In a Hall measurement, R_{xy}, voltage is measured perpendicular to current flow.

The resistance of a 2DES strongly depends on $B_\perp$. Directional resistance measurements undergo Shubnikov-de Haas (SdH) oscillations as a function of the magnetic field strength, which are a result of the Landau levels shuffling past the Fermi level as the magnetic field is increased and the filling factor falls. Figure 2.6, a typical directional transport curve for a high mobility sample, provides a good illustration of SdH oscillations. SdH minima occur when ν is an integer and the Fermi level lies between spin split LLs. Maxima occur when ν is half-integer and the Fermi level lies in the center of a spin split LL, though other features arise to alter the maxima in the low LLs.

Hall resistance measurements yield a straight line, as expected, with $R_{xy} = \frac{1}{eN_s}B_\perp$. However, this line contains plateaus about each integral value of ν, with $R_{xy} = \frac{h}{e^2\nu}$. These features compose the integer quantum Hall effect (IQHE), and the plateaus can be explained by 1D chiral LL edge states and disorder-induced localization (see [2]). Of note, the quantized value $\frac{h}{e^2} = 25,812.807\ \Omega$ now sets the standard for the Ohm. The IQHE is also used for precision measurement of the fine structure constant α. Interestingly, disorder promotes broad Hall plateaus, and so a less-than-high mobility is ideal for displaying the IQHE.

On the other hand, Hall measurements on high mobility samples produce even more plateaus in the Hall resistance, though at non-integer filling factors. These plateaus comprise the fractional quantum Hall effect (FQHE), which differs greatly from the IQHE. The extra features altering the low LL SdH maxima in figure 2.2, especially the dips between roughly $B_\perp = 4$ and 5 Tesla, are manifestations of the FQHE. The initial discovery of the FQHE found plateaus at only odd-

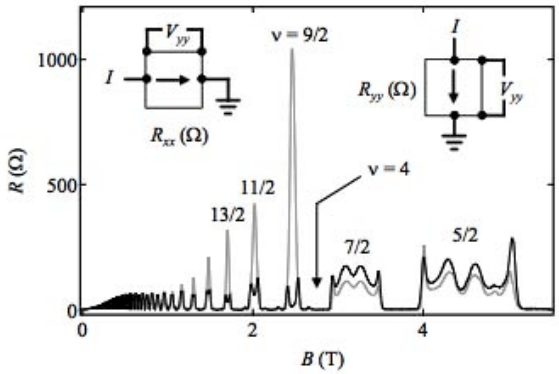

Figure 2.3: *Experimental signature of the stripe state at T = 25 mK in the magnetotransport of a high mobility 2DES. R_{yy} (black) corresponds to [110], and R_{xx} (grey) to [1$\bar{1}$0]. Picture adapted from [6].*

denominator values of ν. Subsequent work demonstrated the FQHE with even-denominators. The FQHE is due to inter-electron interactions and can be interpreted as the IQHE for fractionally charged composite fermion and boson quasiparticles [2].

2.4 The Stripe State

The anisotropic stripe state is a high LL oddity occurring at half-integral filling factors in the $N \geq 3$ LLs: $\nu = {}^{9}/_{2}, {}^{11}/_{2}, {}^{13}/_{2}$, etc. Characterized by a large difference between conduction along two orthogonal in-plane crystallographic axes, this effect gets its name from the suspicion of a stripe-patterned charge density wave (CDW) formation. Figure 2.3 demonstrates the experimental signature of the stripe state. Figure 2.4 provides a sketch of the stripe state. The parallel stripes consist of alternating regions with local filling factors that alternate between the two nearby integer filling factors. Resistance anisotropy follows from the relative difficulty of conduction across the stripes versus the ease of conduction along the stripes. The stripe state occurs with T $\lesssim$ 100 mK and in the highest quality samples with $\mu \gtrsim 10$.

There are two theories about the formation of the stripe state. In the first, anisotropy results from spontaneous arrangement of the 2DES density into a unidirectional striped pattern [4]. In the

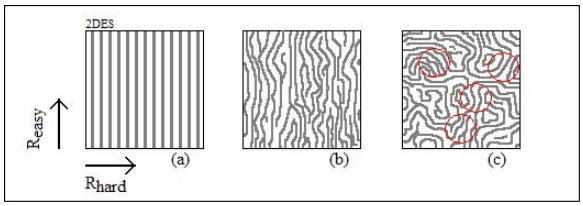

Figure 2.4: *Sketches of the stripe state. (a) CDW stripes. (b) Phase transition stripe "melting." (c) Local domain formation in phase transition picture. Red circles highlight a few local domains.*

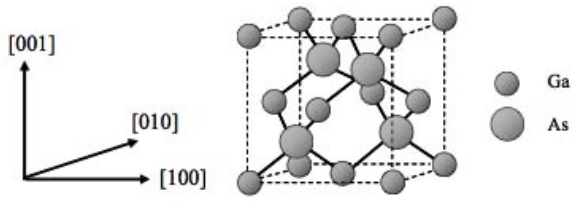

Figure 2.5: *GaAs unit cell and crystallographic axes. [110] and [1$\bar{1}$0] are the unit vectors formed by the sum and difference, respectively, of [100] and [010]. Picture adapted from [6].*

second, the global stripe pattern emerges from the alignment of initial local domain stripe patterns through an isotropic-to-nematic phase transition (figure 2.4 (b) and (c)) [7].

Interestingly, the stripe state resistance anisotropy always orients along one of two in-plane crystallographic axes of the host GaAs/AlGaAs material, with the "hard" direction along [1$\bar{1}$0] and the "easy" direction along [110]. Figure 2.5 depicts the relationship between these crystallographic directions and the structure of GaAs. The identity of the orientation mechanism responsible remains hidden [5].

The addition of an in-plane field aligns the "hard" resistance direction of the stripe state with the direction of the applied in-plane field, and replaces the $\nu = 5/2$ and $7/2$ FQHE with stripe state anisotropy [8, 9]. We conducted a SURF project during the summer of 2004 to test the effects of an in-plane magnetic field on the formation of the stripe state at the relatively high temperature of T = 0.3 K. We used tilt to create an in-plane magnetic field along the [110] crystallographic axes of two samples, such that any anisotropy induced would be reversed from the normal orientation. Figure 2.6 is an overlay of data at $\nu = 5/2$ with different tilting angles for a sample from the same wafer as used in this project. Our data illustrated an increase in anisotropy in the expected orientation with increased tilt in the $N \geq 3$ LLs and at $\nu = 5/2$ and $7/2$, suggestive of the onset of stripe state formation in both samples ($\mu = 2$ and 9) at the high temperature T = 0.3 K.

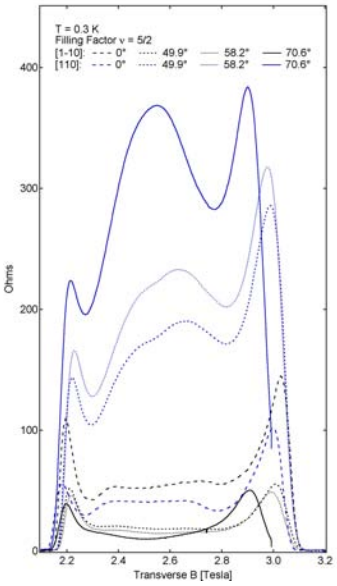

Figure 2.6: *SURF 2004 tilted field experiments illustrating onset of possible stripe anisotropy with increased tilt at filling factor ν=5/2. (Tilt $\pm$ 0.5°).*

2.5 Project Motivation: Stripe State Orientation Mechanism

The host material at the location of the 2DES in a heterostructure is symmetric with respect to inversion of the [110] and [1$\bar{1}$0] axes. Therefore, no directional preference differentiating these two

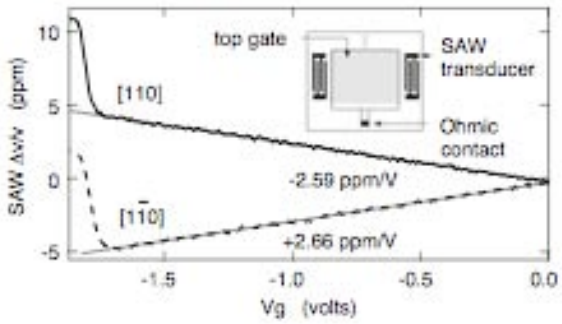

Figure 2.7: *Surface acoustic wave fractional velocity shift at 671 MHz and T = 0.3 K. The linear region results from the piezoelectricity of GaAs in response to a top-gate voltage. The nonlinear region for low V_g arises from sample depletion. Picture adapted from [10].*

axes should arise from the host material. Regardless, the stripe state anisotropy naturally orients in one particular arrangement: the "hard" direction along $[1\bar{1}0]$ and the "easy" direction along [110]. Therefore, an unidentified symmetry-breaking field responsible for the consistent stripe orientation in the absence of external symmetry-breaking mechanisms, such as an in-plane magnetic field, exists.

We know that this native symmetry-breaking field contains both a $\cos(2\theta)$ and $\cos(4\theta)$ term, where θ is a polar angle in-plane with the 2DES. Bulk GaAs crystal symmetry permits the $\cos(4\theta)$ term, but prohibits the $\cos(2\theta)$ term. Thus the origin of the in-plane symmetry-breaking $\cos(2\theta)$ term is a mystery. We suspect, however, that the loss of "top-down" inversion symmetry inherent in the sample structure due to the proximity of a free surface to the 2DES may play a role in this term.

Two recent results provide support that the loss of in-plane inversion symmetry due to a $\cos(2\theta)$ distortion is key to stripe orientation. First, an experiment using a perpendicular electric field to alter the 2D carrier density observed an abrupt interchange of the anisotropy axes at $\nu = 9/2$ about a transitional density [11]. This application of an electric field by a gating electrode breaks top-down inversion symmetry. Second, we observed that the presence of a perpendicular electric field induced a $\cos(2\theta)$ distortion in the propagation of surface acoustic waves (SAWs) on GaAs heterostructures (figure 2.7) [10]. This effect results from the piezoelectric properties of the GaAs substrate: a gate potential applies pressure along the transverse crystal axis resulting in unequal strains along the two in-plane crystal axes, breaking in-plane inversion symmetry. Therefore, gate induced sample strain may be responsible for the tunable density observation.

To investigate this matter, we proposed to examine the effects of $\cos(2\theta)$ distortion on the stripe state orientation directly. We planned to induce $\cos(2\theta)$ distortion through the application of uniaxial strain (appendix A.4), using the novel approach demonstrated by M. Shayegan [1] of the application of commercial piezo-actuators for applying *in situ* uniaxial strain on semiconductors at low temperatures [1]. The method consists of epoxying a thinned 2DES sample onto a piezo-

actuator, along with strain gauges for precise strain measurement. The main advantage of this approach is that the amount of strain may be controlled during measurement, without the need for thermal-cycling. As a result, we can simulate gate-induced sample distortion through uniaxial strain application.

If strain application influences the anisotropy orientation, then we have direct evidence that loss of in-plane inversion symmetry plays a key role in the field orienting the stripe state. Moreover, if some amount of strain causes the anisotropy axes to abruptly interchange, then we will have suggestive evidence that the density-induced effect in [11] results from gate-induced sample distortion and that the structural loss of top-down inversion symmetry may be responsible for the native symmetry-breaking field.

2.6 Strain and Two-Dimensional Electron Systems

Before we can apply the uniaxial strain technique on the stripe state, we must determine the effects of uniaxial strain on 2DESs in the absence of the stripe state. We proposed to carry this out empirically, en route to our end goal.

A review of the literature did not produce a quantitative result of the effects of uniaxial strain on the bulk properties of 2DES heterostructures, likely as a result of the difficulty of such measurements. However, there are experiments which show that the application of hydrostatic pressure changes the carrier density N_s and g-factor of a 2DES. Even in this case, the mechanism behind the density variation is not well understood [12, 13, 14].

Intuitively, we can imagine many reasons why the application of strain should have an effect on 2DESs. Strain could have an effect on the 2DES resistance in the same manner as it would on a thin metal film. We could also imagine strain to effect the band gap alignment of the dissimilar materials in the GaAs/AlGaAs heterostructure, which would change the carrier density N_s in the analogy of how changing the voltage of a capacitor alters its charge density. Nevertheless, for successful completion of this project, the effect of uniaxial strain on 2DESs must be determined before a detailed study of the stripe state may begin.

Chapter 3

Experimental Methods

This chapter gives an overview of the experimental setup of the project. The appendices provided at the end of this document provide more in-depth detail when appropriate. All equipment and 2DES samples used belong to the Eisenstein group, under which all research was supervised.

3.1 Two-Dimensional Electron System Samples

The 2DES samples studied in this experiment are modulation doped GaAs/$Al_xGa_{1-x}As$ (abbreviated GaAs/AlGaAs) heterostructures grown by L. N. Pfeiffer and K. W. West at Bell Laboratories using molecular beam epitaxy (MBE). One wafer, with $x = 0.24$ and $\mu \simeq 9$, provided all the samples used for the completed piezo-headers (PHs). In this wafer, the 2DES is confined at an internal single-interface heterojunction, as depicted in figure 3.1. PH-11, which is currently under construction, will use a sample from a different wafer, with a higher mobility of $\mu \simeq 14$. This wafer differs from the previous one in that it confines the 2DES inside a 300 Å wide quantum well.

3.1.1 Processing

Typical samples measure 5×5 mm^2, and are cleaved by hand along the natural crystallographic axes [110] and [1$\bar{1}$0]. Figure 3.2 illustrates a typical cleaved sample. A Methanol-Bromine etching process thins the 2DES samples from $^1/_2$ mm down to 120-150 μm, ensuring that strain is fully transmitted

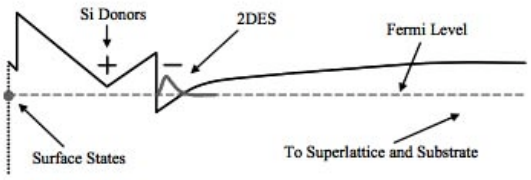

Figure 3.1: *Single-interface heterojunction 2DES band diagram. The horizontal axis depicts the location within the sample thickness, with the top surface on the left and bottom surface (not shown) on the right. Picture adapted from [6].*

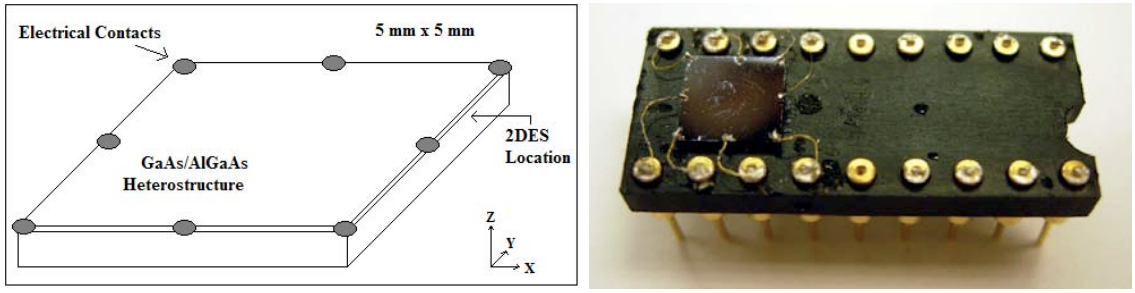

Figure 3.2: *Typical 2DES sample. (left) Sketch of a cleaved and contacted sample. (right) Wired-up sample on an 18-pin header.*

through the entire sample [1]. For some samples, we used photolithography to etch the 2DES down to a $\frac{1}{2} \times \frac{1}{2}$ mm^2 mesa. Mesa-etching reduces the area of the 2DES by a factor of 100, increasing the strain homogeneity throughout the 2DES. Figure 3.3 shows two mesa-etched samples.

Eight annealed peripheral contacts at the corners and midpoints of the 2DES edge provide an electrical interface to the sample. Hand-placed indium solder dots are used for non-mesa etched samples, while evaporated Ni/AuGe contacts are used for mesa etched samples. Gold wires 0.002" thick attach these contacts to an eighteen pin dual-in-line electrical header for easy interfacing, as in figures 3.2 and 3.3. Please see appendix D for more detailed information about sample processing.

3.1.2 2DES Electrical Measurement

We probe 2DES samples through electrical measurements, using very small alternating current (I $\simeq$ 100 nA, $f \sim 13$ Hz) in order to minimize any heating effect on the 2DES. Four-terminal electrical measurements of the directional and Hall resistances performed with an EG&G/Princeton Applied Research model 124A lock-in amplifier determine the main 2DES sample characteristics: zero-field ($B_\perp = 0$) resistivity per square ρ ($\Omega/\square$), carrier density N_s (10^{11} cm^{-2}), and mobility μ (10^6

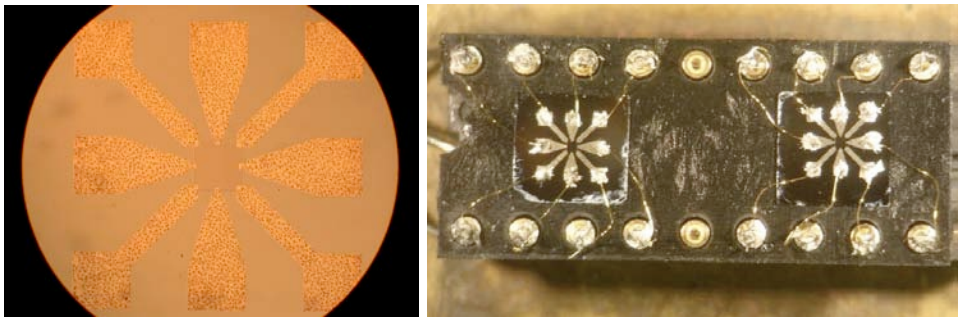

Figure 3.3: *Mesa-etched samples. (left) Microscope picture of the top of the sample used in PH-9 after annealing, but before wire-up. The 2DES mesa is the small square in the very center. The spotted structures are the evaporated contact pads. (right) Mesa-etched samples, before use on PH-9 and PH-10, wired-up together on a header.*

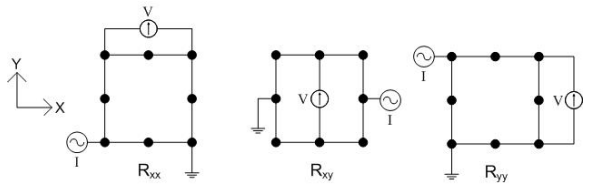

Figure 3.4: *Typical four-terminal contacts arrangements for electrical measurement.*

cm^2/Vs). Figure 3.4 depicts typical arrangements of sample contacts for these measurements. The lock-in averages its output with a time constant of 0.3 seconds, and a computer records the lock-in output every 0.9 seconds during measurement. Samples are illuminated once briefly with a red light emitting diode following cool-down and before measurement to increase N_s.

The resistivity per square ρ of a sample is determined by zero-field directional resistance measurements using the Van der Pauw method [15, 16]:

$$\rho = \frac{\pi d}{ln(2)} \frac{(R_{xx} + R_{yy})}{2} f(\frac{R_{xx}}{R_{yy}})$$

The function f is a geometric correction factor given in [15].

Sample magnetotransport can determine the carrier density N_s in two ways. First, from the slope of the plot of $(\nu_{min}, \frac{1}{B_\perp})$ for the SdH minima, where ν_{min} are integers:

$$N_s = \frac{h}{e} \left(\frac{\frac{1}{B_\perp}}{\nu_{min}} \right)$$

Second, from the average slope of the Hall resistance as a function of the magnetic field $B_\perp$, for $B_\perp \lesssim 0.5$ Tesla:

$$N_s = \frac{1}{e} \left(\frac{B_\perp}{R_{xy}} \right)$$

Finally, we use ρ and N_s to calculate the sample mobility μ:

$$\mu = \left(\frac{1}{e \ \rho \ N_s} \right)$$

3.2 Cryogenics

We cool to T = 4.2 K by immersion in liquid ^{4}He using "dipping sticks" that facilitate electrical connection to the sample while cold. One dipping stick contains a small superconducting magnet capable of roughly 0.52 Tesla, which is used for all T = 4.2 K tests requiring transverse magnetic fields.

We reach T = 0.3 K using a top-loaded ^{3}He cryostat complete with a superconducting magnet capable of 9 Tesla. To gain enough room to fit PHs into the fridge, we use a modified end-cap for one

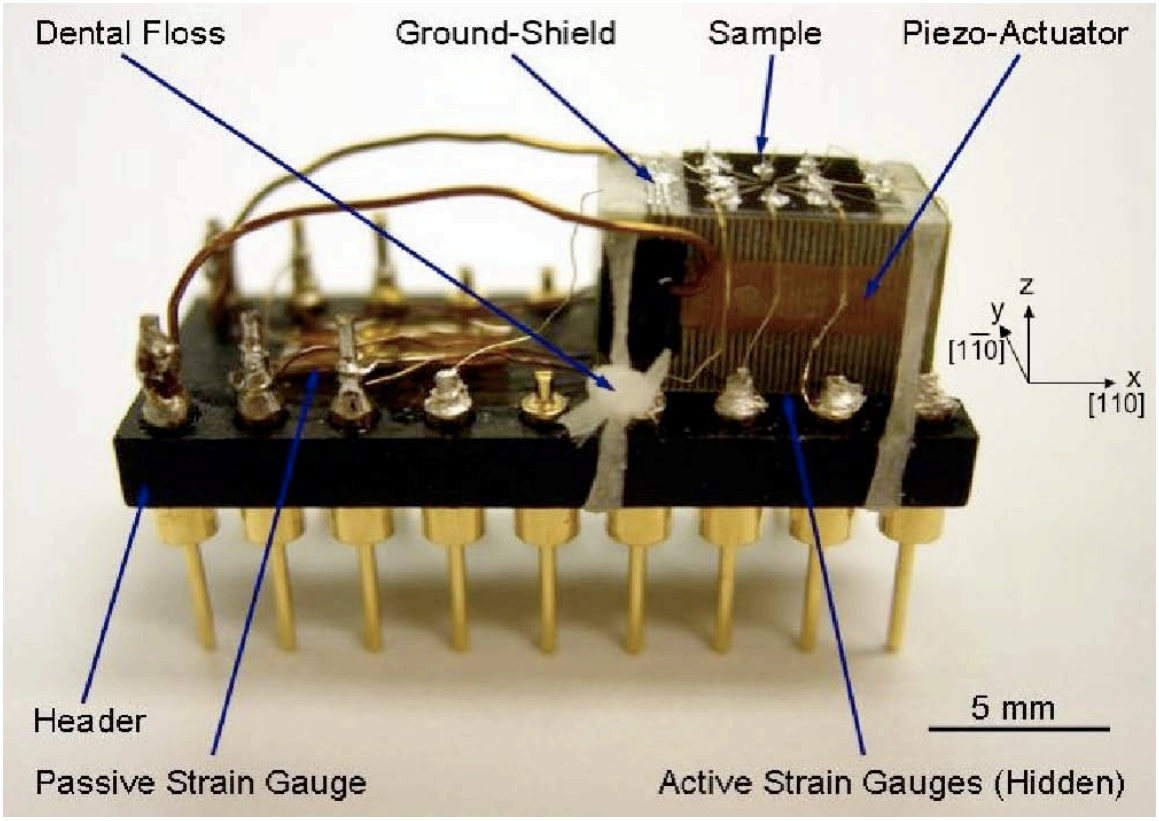

Figure 3.5: *Side profile of PH-9 with the individual components labeled. Pin 18 is front right.*

of the top-loading sticks which, coincidentally, we built for my 2004 SURF project to accommodate a tilting-sample header.

3.3 Piezo-Header Method

We have built ten piezo-headers in succession, with an eleventh currently under construction. This section describes our current approach towards constructing and operating piezo-headers.

3.3.1 Design

Figure 3.5 gives a breakdown of the components of a working PH, and figure 3.6 shows the electrical hook-up of a PH. The base is an 18-pin electrical header, which provides a convenient mechanical and electrical interface. The heart of the PH is the piezo-actuator, which we use to strain a 2DES sample. A perpendicular strain gauge pair attached to the under-side of the piezo-actuator measures the strain applied to the sample both along (ϵ_x) and perpendicular (ϵ_y) to the poling direction (x) of the piezo [1]. A two-part epoxy secures the gauges to the actuator, with the x-gauge placed closest to the actuator. Vacuum impregnation of the thin epoxy layer bonding the gauges to the actuator removes

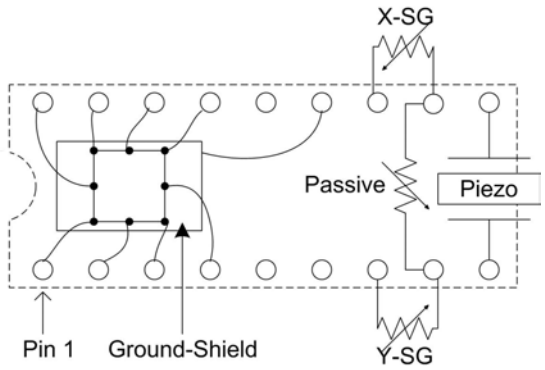

Figure 3.6: *Electrical diagram of PH pin and component arrangement. NOTE: Components are not arranged physically as they are on an actual PH. Here, SG is an abbreviation for strain gauge.*

bubbles, which could affect strain measurement. Minimization of epoxy use prevents unnecessary loading of the piezo-actuator. A free-standing strain gauge is attached to the header for temperature compensation during strain measurement. To shield the 2DES from any electric fields from the piezo-actuator, an aluminum ground-shield layer is evaporated on to either the piezo-actuator surface or the sample underside (to be tried on PH-11) and connected to a pin on the header. A processed and characterized sample is epoxied to the face of the actuator opposite of the strain gauges, and wired up to the header. Finally, dental floss secures the piezo-actuator to the header in order to prevent vibration and misalignment.

Samples are aligned with [110] along the poling direction (x) of the piezo-actuator. The crystal axes are determined before processing through optical examination of surface imperfections characteristic of our heterostructures. We adhere to this alignment convention since we are uncertain if the effects of uniaxial strain are alignment dependent. For shorthand, we refer to the two in-plane crystallographic axes and uniaxial strain directions using x and y:

$$\begin{cases} x \equiv [110] \\ y \equiv [1\bar{1}0] \end{cases}$$

Please see appendix C for more detailed information about PH construction.

3.3.2 Piezo-Actuator Control

The piezo-actuators are controlled using a dc power supply and an inline 5 megohm current-limiting protection resistor, as displayed in figure 3.7. Power supply polarity is manually reversed as necessary. Care is taken when changing the bias voltage to account for the response time of an actuator. We found a sweep speed of 1 volt per second to be sufficiently slow to avoid creep issues.

Please note that there are two orientations for the piezo-actuator hook-up. Piezo-actuators are

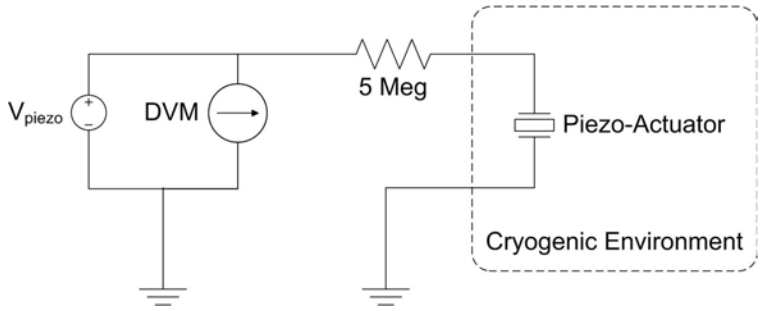

Figure 3.7: *Piezo-actuator control circuit. Polarity of the power supply voltage is controlled manually by reversing the power supply leads as needed. Please note that the piezo-actuator is a polar device, and that there are two orientations for it in this circuit. Here, DVM refers to a digital voltmeter.*

polar devices, and switching between the two orientations changes the sign between the applied voltage and resultant strain. One lead of the piezo-actuator is grounded, and so the orientation of the piezo-actuator leads and power supply polarity determined the sign of the gating voltage that the piezo-actuator would apply on a sample in the absence of a ground-shield. This detail means that gating and strain effects are differentiable by swapping the hook-up of the piezo-actuator leads, thereby altering the sign between the two effects. For example, on a graph of a measurement with the piezo bias voltage on the x axis, swapping the leads hook-up would reverse any strain-induced effects from left to right about zero-bias voltage.

3.3.3 Strain Measurement

PHs incorporate three strain gauges: two "active" gauges on the underside of the piezo-actuator and one "passive" free-standing gauge. A picture, such as figure 3.8, of the active gauges of every PH is taken after attachment to the piezo-actuator in order to record the gauge alignment. Though the gauges are manually attached, alignment is typically true to within a few degrees. The three strain

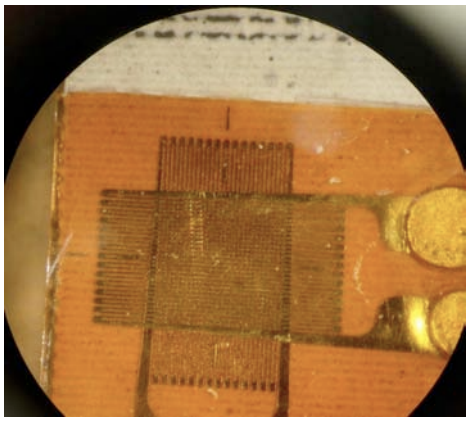

Figure 3.8: *PH-9 active strain gauges. Alignment is measured by comparing the strain gauge traces and the piezo-actuator layers (near-horizontal lines). Please note that the picture is angled.*

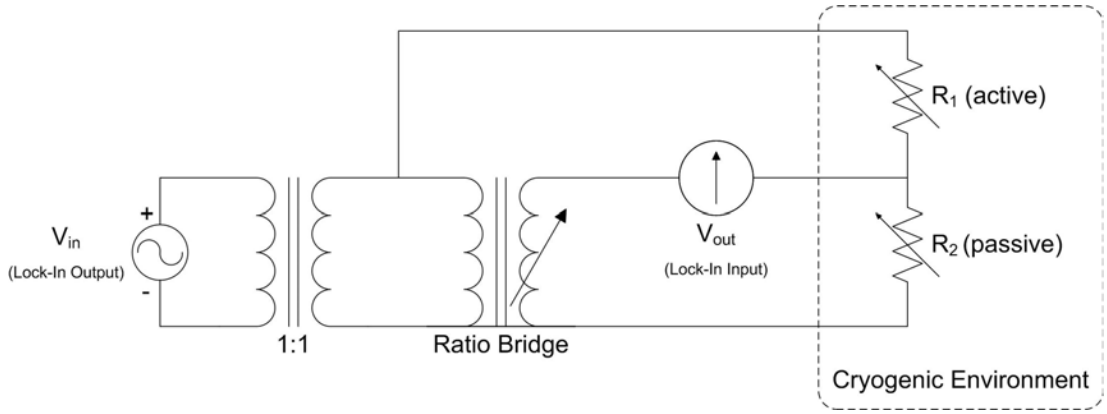

Figure 3.9: *Simplified Wheatstone half-bridge strain measurement circuit. R_1 is replaced with either the x or y strain gauge, and R_2 by the passive strain gauge, during measurement. Ground reference for the bridge is placed at the ratio bridge output.*

gauges on a PH are wired together as depicted in figure 3.6. The passive gauge and one active gauge are used together to measure either ϵ_x or ϵ_y.

A lock-in amplifier and homemade Wheatstone half-bridge facilitate strain gauge measurement. Figure 3.9 gives a simplified circuit diagram. A lock-in amplifier excites the bridge with a constant voltage V_{ex} at about 100 Hz, and measures the bridge output V_{out}, with the same time averaging and data acquisition as used for sample measurement. An inductive ratio-bridge is used for bridge nulling. The passive is used in the half-bridge arrangement to compensate for the thermal sensitivity of the active gauge. As a result, strain can be accurately measured as long as the magnetic field is held constant. Equation B.6 from appendix B gives the bridge output after nulling, where N_o is the ratio bridge setting and GF is the strain gauge gauge-factor:

$$\frac{V_{out}}{V_{in}} = -\left[N_o(1-N_o)GF\right]\epsilon \approx -\frac{1}{2}\epsilon$$

Measurement at different temperatures requires different excitation voltages, due to heating power restrictions of different cooling methods. In typical operation for T = 4.2 K, $V_{ex} = 1/2$ V. For T = 0.3 K, typically $V_{ex} = 0.01$ V, to keep the strain gauge heat output below roughly a μW. This low V_{ex} requires the use of a 100:1 pre-amp ratio transformer in the lock-in amplifier to measure the bridge output. We calibrate the bridge as a whole by measuring the output after nulling in response to changing the ratio bridge. Please see appendix B for more detailed information about strain measurement.

3.3.4 PH 2DES Measurement Procedure

During thermal-cycling, there is a choice of either shorting the piezo-actuator leads, or leaving them open. Cooling the PH with the piezo-actuator leads shorted will protect against potentially

hazardous voltages generated by the piezo-actuator. However, doing so will result in large amounts of frozen-in strain in the sample once cold. Cooling with the leads open, on the other hand, does not result in large frozen-in strain. Therefore, the best method is to thermally cycle the PH with the piezo-actuator leads open, taking care to thermally cycle gently. By the nature of our immersion, our T = 4.2 K tests are not very gentle, and so were only used on the early PHs. Using a cryostat, we typically cool to T = 0.3 K in about forty-five minutes.

Our current methods can be used to measure strain while the PH is cold and the magnetic field strength is held constant. Unfortunately, we cannot measure strain during large thermal changes or during changes in magnetic field strength. Thus, the amount of frozen-in strain from cool-down cannot be measured with the PH strain gauges. In order to minimize heating, strain measurement is usually performed during few tests, and primarily only to calibrate the piezo-actuator. The piezo-actuator is calibrated through a stroke test at a fixed magnetic field, where the piezo bias voltage is swept in a triangle wave, typically with a speed of 1 volt per second. The effects of strain and piezo bias voltage gating can be separated by altering the orientation of the piezo-actuator in the piezo control circuit, as mentioned in section 3.3.2.

A typical data run for a PH test following cool-down consists of the following:

1. Characterize sample before strain application.
2. Calibrate piezo-actuator.
3. Measure zero-field R_{xx} and R_{yy} vs. strain.
4. Measure the sample density vs. strain using R_{xy}.
5. Measure magnetotransport at fixed strain.

Step 1 allows for a later comparison to see if *in situ* strain application altered the sample. Steps 3 and 4 give the directional resistance and carrier density N_s for the sample as a function of strain. Step 5 produces the transport as a function of applied strain. Of course, in practice the tests performed vary for every PH and every cool-down.

Chapter 4

Piezo-Header Results

This chapter gives a chronological overview of the refinement of the piezo-header (PH) method, and a summary of the performance of the current PH design.

4.1 2005 SURF

We built six PHs in a succession during ten weeks last summer. We performed T = 4.2 K tests on the first four PHs (figure 4.1 (left)), and T = 0.3 K tests on the last two PHs of this batch (figure 4.1 (right)). We did not incorporate ground-shields into these initial versions, as we decided it was too early to incorporate that step into our PH construction process. Thus our 2DES measurements from these PHs suffered from piezo bias voltage gating. Tests were performed with the piezo-actuator leads shorted during thermal-cycling, as it was not until very recently that we learned to cool with the leads open.

The first two PHs, PH-1 and PH-2, were very minimal, each consisting of a non-cryogenic piezo-actuator with two orthogonal strain gauges mounted on an 18-pin header. We used both primarily for our most initial construction and strain measurement tests. These were the only actuators to be used at room temperature. Figure 4.2 shows the room temperature strain calibration of PH-1. Both piezo-actuators failed after thermally-cycling back to room temperature following T = 4.2

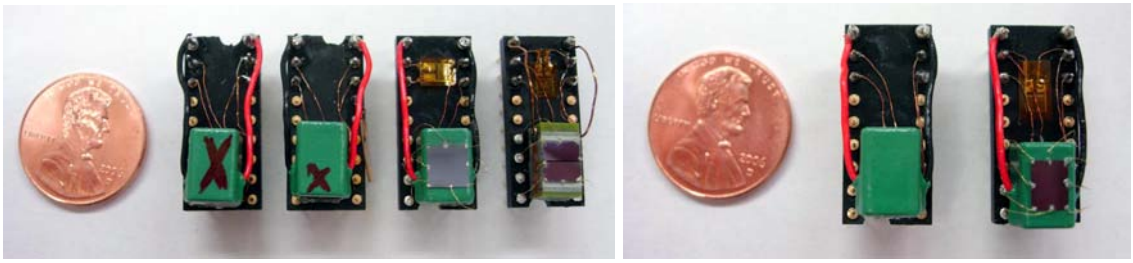

Figure 4.1: *SURF 2005 PHs. (left) PH-1 to PH-4 in order from left to right. A crack is visible in PH-4, which is explained later. (right) PH-5 and PH-6.*

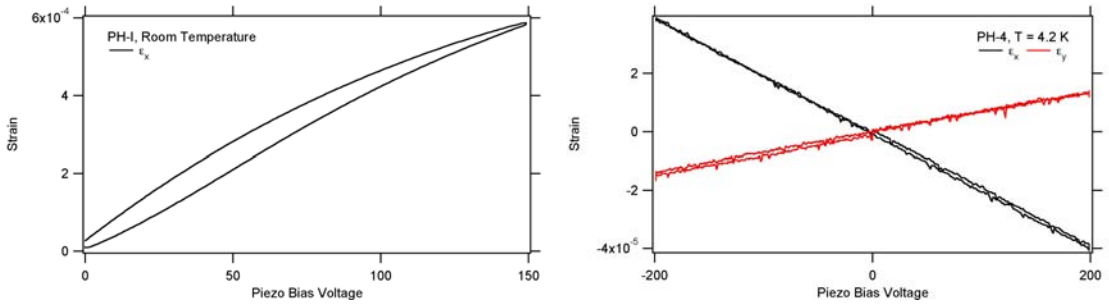

Figure 4.2: *Effects of temperature on PH performance. (left) PH-1 stroke curve at room temperature, with expected hysteresis. (right) PH-4 stroke curve at T = 4.2 K. Notice that at cryogenic temperatures, the hysteresis is heavily attenuated.*

K immersion, suffering from internal electrical breakdown which we would learn later came from insulation cracking (figure 4.3 (left)). We first incorporated a sample in PH-3, which was the next evolution of the previous two PHs. Unfortunately, its strain gauge was damaged, and it suffered the same fate as the previous two PHs.

We made a major advance with PH-4, which utilized a cryogenic piezo-actuator and also featured a sample. PH-4 worked reliably at T = 4.2 K, and was tested successfully in the presence of magnetic fields strengths of up to ½ Tesla. Figure 4.2 displays the strain calibration of PH-4 at T = 4.2 K. PH-4 even survived repeated thermally cycling. However, PH-4 broke when an accidental over-voltage nearly cracked its piezo-actuator in half (figure 4.3 (right)).

From the PH-4 tests, we verified the expected effects of low temperatures on piezo-actuators: At the price of a reduction in strain output, the piezo-actuators lose the majority of their hysteresis and develop the ability to operate bipolar. In other words, low temperatures linearize the output of the piezo-actuators, and allow for the piezo-actuator to produce both positive and negative strain.

We assembled PH-5 and PH-6 to test the use of non-cryogenic piezo-actuators at T = 0.3K in a ^{3}He cryostat. PH-5 and PH-6 were reproductions of PH-2 and PH-3, respectively. We used

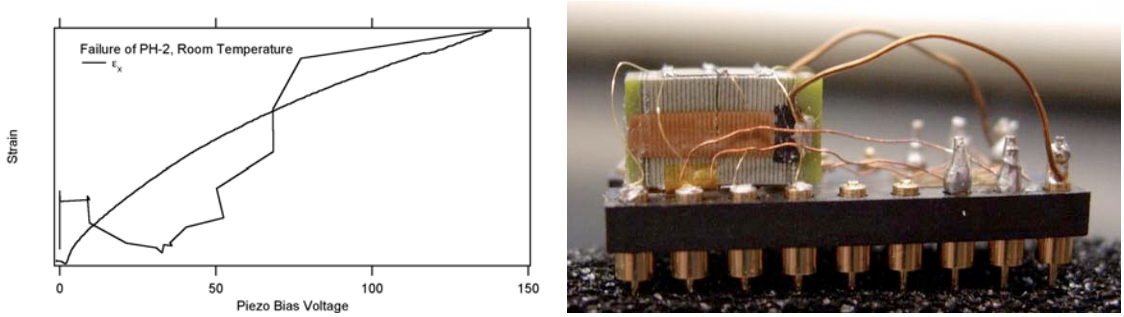

Figure 4.3: *PH-2 and PH-4 failure. (left) PH-2 failure during stroke curve at room temperature, following T = 4.2 K test. The piezo-actuator failed at 150V, shorting the power supply and sending the strain back to zero. (right) PH-4 crack from accidental over-voltage during T = 4.2 K test.*

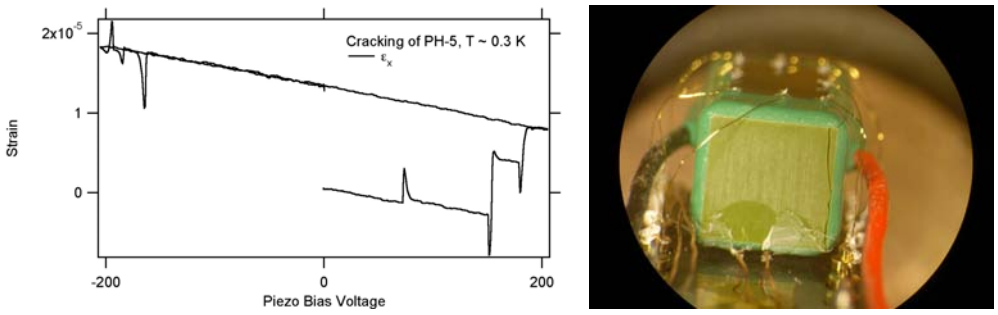

Figure 4.4: *Cracking. (left) Cracking signature in stroke curve for PH-5 during first tests at T = 0.3 K. (right) Large crack on PH-6 resulting from T = 0.3 K test. Upon closer examination, we found hairline cracks along all edges of each non-cryogenic piezo-actuators we had used.*

PH-5 to test the more gentle vacuum cooling of the ^{3}He cryostat, and it "survived" two thermal-cycles. Its strain calibration at T = 0.3 K displayed cracking, which we initially interpreted as strain measurement error (figure 4.4 (left)). Thinking PH-5 worked, we proceeded with a test of PH-6. Due to contacts troubles, we were only able to perform Hall measurements, which reproduced the effects seen by PH-4 but to a much smaller degree. Upon warming and inspecting PH-6, we discovered a crack in the piezo-actuator (figure 4.4 (right)). This discovery prompted a more careful examination of all the previous PHs which used a non-cryogenic piezo-actuator. We found that thermal cycling of the non-cryogenic piezo-actuators to cryogenic temperatures produced hairline cracks along the edges of *all* of the piezo-actuators used, with the largest appearing on PH-6. Therefore, we learned that we must use the cryogenic piezo-actuators. Also, through working with PH-5 and PH-6, we began to adapt our T = 4.2 K strain measurement setup to suit the ^{3}He cryostat, which posed many challenges to strain measurement. In the end, the initial work with the first six PHs developed a successful initial construction technique and measurement processes.

4.2 Physics 78

We have built four more PHs, PH-7 to PH-10, so far during the school year. Another PH, PH-11, is currently under construction. Each of these used a new type of strain gauge, the XY11, as mentioned in C.1. We continued to cool-down with the piezo-actuator leads shorted during tests, up until the very last set of data taken for repeated trials of PH-9. The PH design changed abruptly after PH-7 to the current approach. We had trouble implementing a ground-shield on PH-9 and PH-10. We hope a new approach will resolved the ground-shield issues in PH-11. Throughout the year, we have continually refined the Wheatstone bridge strain measurement process.

We built PH-7 to reproduce PH-4 for T = 0.3K tests. (The dental floss on Ph-7 shown in figure 4.5 was added after the first cool-down.) It's strain gauges failed, most likely due to incomplete attachment attachment. Magnetotransport showed SdH beating, which is a signal of in-homogeneous

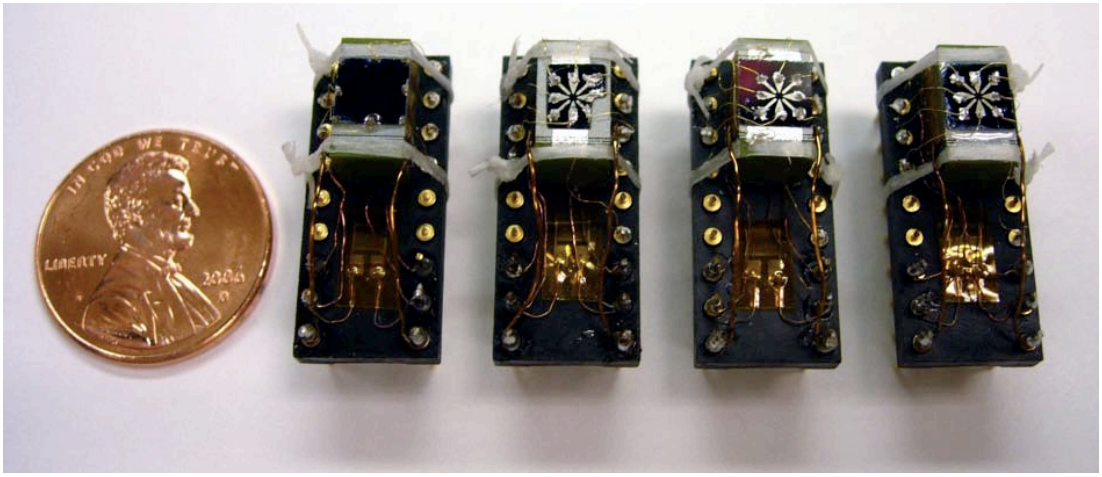

Figure 4.5: *Physics 78: PH-7 to PH-10 in order from left to right. PH-11 (under construction) not shown.*

sample density (figure 4.6 (left)). We interpreted this data to suggest that the strain distribution must be non-uniform throughout the 5×5 mm^2 sample, and so we chose to mesa-etch all further samples to increase strain homogeneity. However, SdH beating was not removed by mesa-etching, and instead was only attenuated when we later learned to cool-down with the piezo-actuator leads open. For example, figure 4.6 displays extremely poor transport and SdH beating in the magnetotransport of PH-10, which has a mesa-etched sample.

We made PH-8 as a first trial of the current PH design, with the hope that the mesa-etching would eliminate the SdH beats of PH-7. Unfortunately the sample cracked through the mesa during cool-down (figure 4.7). We suspect that the crack originated from rough handling during sample processing, only to develop during the cool-down. Nevertheless, we established the procedures for the current PH construction method through working on PH-8, and even constructed an inverted PH holster to facilitate ground-shield evaporation.

We built PH-9 to replace PH-8. During construction the ground-shield developed wrinkles (figure

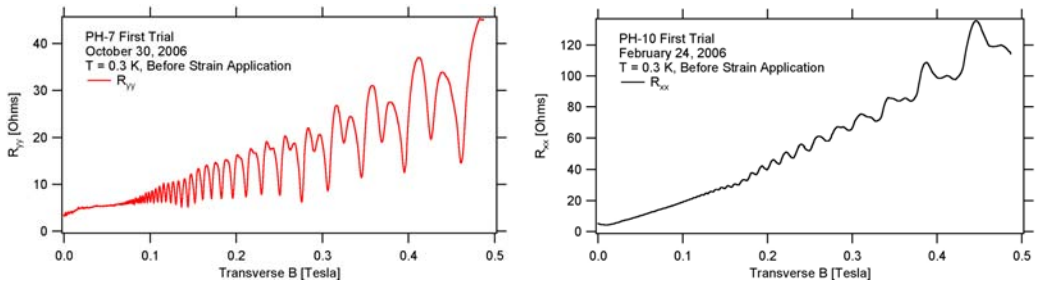

Figure 4.6: *SdH beating from closed-lead cool-down. (left) First observation of SdH beating by PH-7. (right) Particularly poor transport from PH-10. Other contact configurations showed better (and worse) transport.*

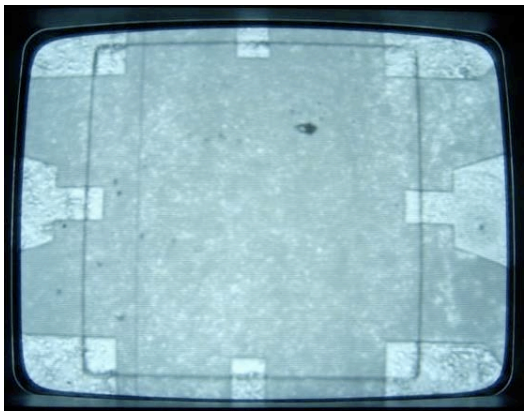

Figure 4.7: *Infrared imaging of the PH-8 mesa. The vertical black line on the left side is a crack.*

4.10 (left)). We went on to finish assembling and testing PH-9, only to find more perplexing sample magnetotransport. We suspected that the ground-shield was responsible, which was not far from the truth, though we would determine why later.

Originally PH-10 was a reproduction of PH-9. The shield-layer on PH-10 also developed wrinkles during construction, so we scraped it off. The removal of the ground-shield on PH-10 damaged the top surface of the piezo-actuator. Luckily, covering the removed portions with a thin layer of epoxy during sample attachment to the actuator effectively fixed the damage. This repair was even approved by the manufacturer.

We took data with the hoped that the comparison of PH-9 and PH-10 would demonstrate the effect of the shielding, but the results were very difficult to interpret and we later found that the ground-shield on PH-9 was broken. During further tests of PH-7, PH-9, and PH-10, we successfully expanded the piezo bias voltage range from ±100 V, which we had previously stayed within out of fear of damaging the PHs, to the maximum rating, ±300 V. Figure 4.8 displays the full range strain calibration for PH-10.

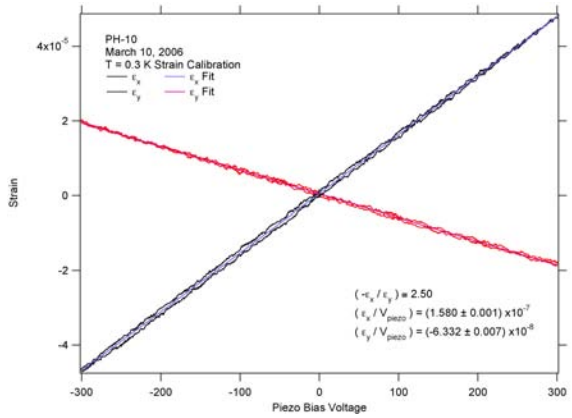

Figure 4.8: *PH-10 strain calibration using full voltage range.*

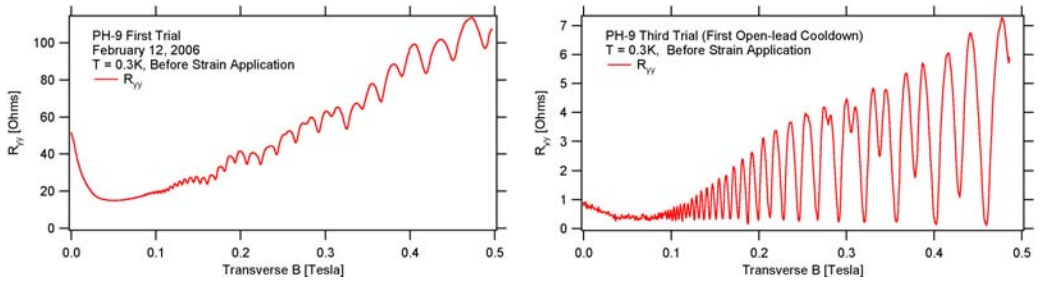

Figure 4.9: *Shorted versus open-lead cooling. (left) Poor transport from shorted-lead cool-down in PH-9 first trial. (right) Normal transport from open-lead cool-down in PH-9 third trial, in which the spin splitting of the LLs is gradually more visible with increased magnetic field.*

The turning point came very recently, when we learned about the differences between open and shorted piezo-actuator lead thermal-cycling. (Thanks to Menser Shayegan for the tip given to Jim at the APS March Meeting!) Cooling the piezo-actuators with their leads shortened, as the manufacturer recommends, results in a large amount of frozen-in strain from the cooling process. Cooling with the leads open, however, does not result in much frozen-in strain. So far, we have only attempted open-lead cool-downs of PH-9. Figure 4.9 demonstrates the drastic difference between the two cool-down approaches for PH-9.

In addition, we then determined that the wrinkles in PH-9, in fact, had broken the ground-shield. We executed a quick repair, as documented in figure 4.10, and performed two more open-lead cool-downs with the repaired PH-9, which form the basis of our knowledge of the effects of uniaxial strain on 2DESs. In these tests, we took advantage of the freedom to choose the sign between strain and piezo bias voltage as discussed in 3.3.2 to verify that our measurements recorded the effects of strain.

4.2.1 PH-11

A new piezo-header, PH-11, is currently under construction. The PH body is complete, but the sample still has to be processed. It will feature a sample from a different, even more high mobility,

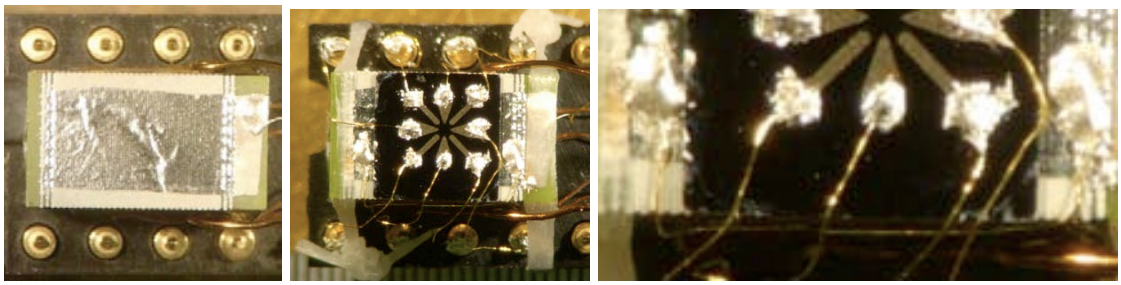

Figure 4.10: *PH-9 ground-shield repair. (left) Wrinkle in ground-shield, before sample attachment. (middle) Picture of the top of the sample and piezo-actuator. (right) Enlargement of the U-shaped wire snaked from the left, down, and over to the right to connect the two opposite sides of the ground-shield.*

wafer, cut to 5x7 mm^2 such that a ground shield layer can be directly deposited on the underside of the sample itself and contacted using the overhang of the extra sample width over the piezo-actuator.

This new sample comes from a wafer known to produce a good stripe state. If the piezo-header construction carries on as planned, then two series of tests will be performed: T = 0.3 K non-stripe state tests, and T $\leq$ 0.1K stripe state tests. This header will hopefully yield the initial goal of this project, and record the effects of manual inversion symmetry breaking through uniaxial strain application on the stripe state.

4.3 Piezo-Header Performance

With our current PH design, we can measure the effects of uniaxial strain on 2DESs at cryogenic temperatures. With open-lead cooling, we can minimize frozen-in strain from cool-down. Our strain measurements are very reproducible, and our piezo-actuator performance is very repeatable. The PHs repeatably thermally-cycle, with the current record held by PH-9 at 5 successful cycles. At T = 0.3 K, using the full range of piezo-actuator bias voltages of $\pm$300 V, we can apply strains of up to about $\pm 5 \times 10^{-5}$). The Poisson ratios for our strain application are typically around 2.5, though they vary between the PHs. The PHs function in the presence of large magnetic field strengths, with our largest tested field at 0.63 Tesla. We have found no indication of a magnetic field strength limit yet.

Chapter 5

2DES Results

This chapter analyzes our measurement of the effect of uniaxial strain on 2DESs through two recent tests with PH-9, performed after ground-shield repair and with open-lead cool-down.

5.1 Data Origins

The first test, which was the fourth overall trial of PH-9, demonstrated that the ground-shield functioned after its repair. The sample magnetotransport was a bit poor following cool-down, so we only performed tests of strain on the zero-field directional resistance of the sample. We verified that the effects observed resulted from strain by changing the hook-up to the piezo-actuator, which alters the sign between strain and gating effects as discussed in section 3.3.2. We observed the data to follow the change of the sign on the strain, confirming that the observed effects resulted from strain.

We performed a second test, which was the fifth trial of PH-9 in total, to double-check our findings. This test reproduced the zero-field directional resistance results of the fourth trial. We

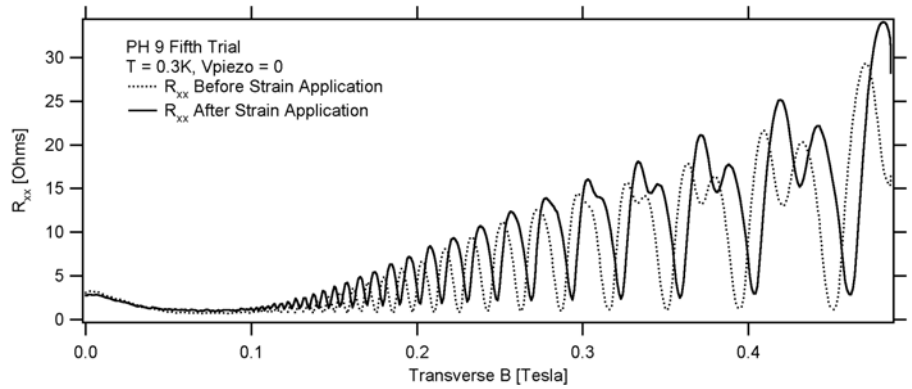

Figure 5.1: *PH-9 fifth trial. Comparison of sample mangetotransport before and after strain application, illustrating a change in the sample. The solid black curve here is the same as the solid black curve in figure 5.6.*

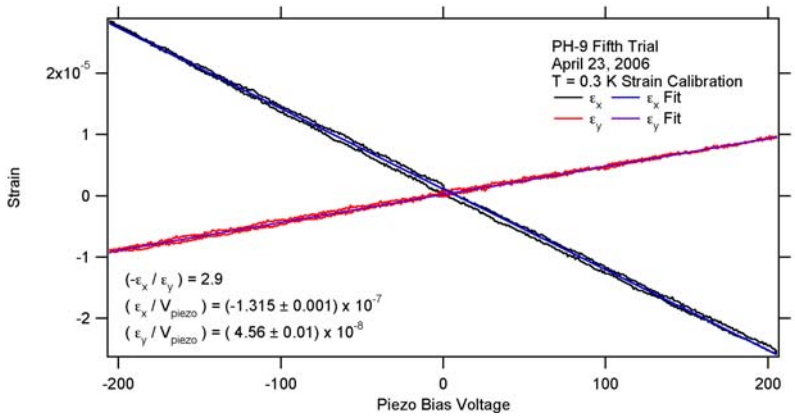

Figure 5.2: *PH-9 fifth trial strain calibration. This graph is the key to all the other graphs in this chapter.*

also continued on to test the magnetotransport in response to strain. We verified that every test resulted from the effects of strain, through altering the piezo-actuator hook-up.

Figure 5.1 shows the magnetotransport of the sample with no applied piezo voltage bias, taken before strain application and later during strained magnetotransport tests. The transport of the fifth trial was very good, as a result from open-lead piezo-actuator cooling. Comparison of the transport at zero piezo voltage bias before and after strain application demonstrates that the strain tests in-between altered the sample, by increasing the sample density by about two percent. Figure 5.2 is the strain calibration key for PH-9, taken right after the first magnetotransport tests. This calibration is the key for converting between strain and piezo bias voltage for the graphs in this chapter.

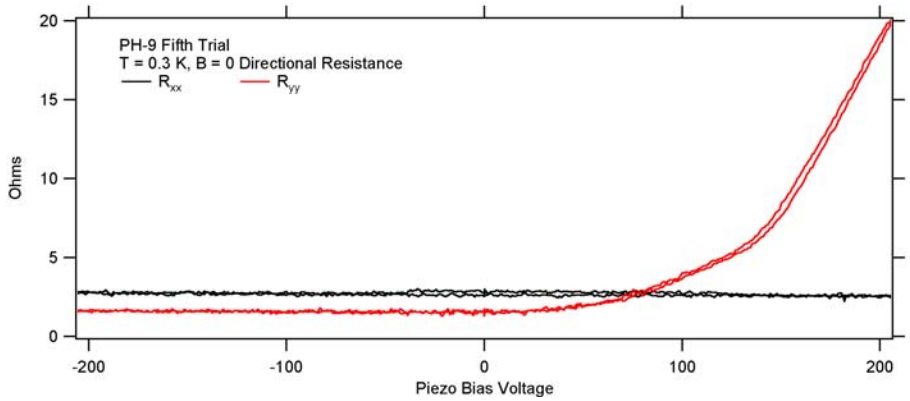

Figure 5.3: *PH-9 fifth trial zero-field directional resistance response to strain. Strain was applied as a triangle wave stroke, which yields closed loop curves with some hysteresis from the piezo-actuator.*

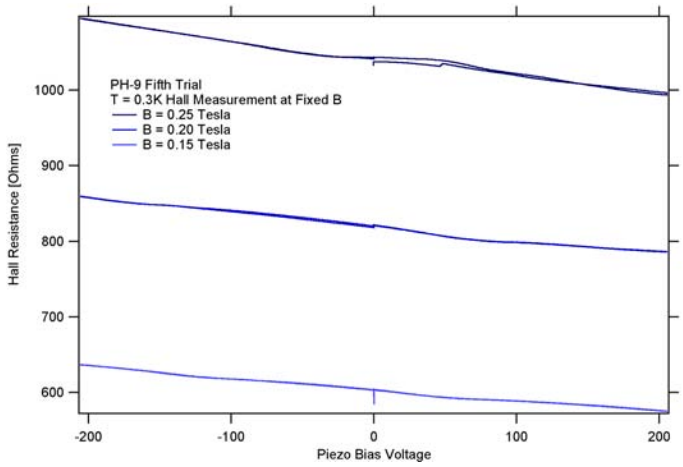

Figure 5.4: *PH-9 fifth trial Hall resistance as a function of piezo bias voltage at fixed B.*

5.2 $B_\perp = 0$

Figure 5.3 illustrates the directional transport of PH-9 under uniaxial strain application. We observed R_{xx} to be roughly unresponsive. However, R_{yy} had a particularly large response to strain application for neggative strain (positive voltage bias), which was observed to swap in accordance with changes in the strain sign and was observed in both the fourth and fifth PH-9 trials.

5.3 Magnetotransport

Figure 5.4 displays the stroke measurement of the Hall resistance under uniaxial strain at fixed magnetic field strengths. From interpolation of this data, we calculated the density of the sample as a function of strain. Figure 5.5 displays our results as a function of piezo bias voltage and principle strain ϵ_x. We observed the sample carrier density N_s to change by about $\mp 4\%$ in response to uniaxial

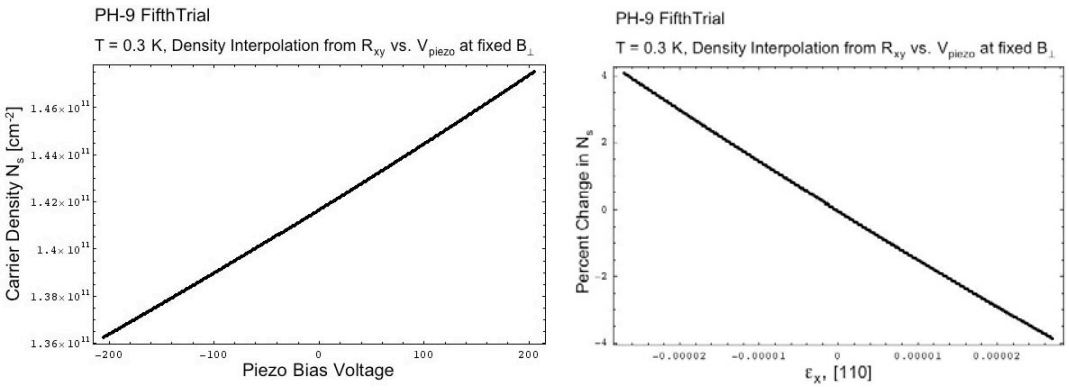

Figure 5.5: *Strain-induced density variation. (left) Carrier density plotted as a function of the piezo bias voltage. (right) Percent change in carrier density plotted as a function of the applied strain.*

strain of $\pm 3 \times 10^{-5}$. The change was very linear, with a slope of $\left(\frac{\Delta N_s}{\epsilon_x}\right) \simeq -2.09 \times 10^{14}$ cm^{-2}, which we can also express as $\left(\frac{\Delta N_s / N_s}{\epsilon_x}\right) \simeq -1.47 \times 10^3$.

We took magnetotransport curves at fixed piezo bias voltages of -200, -100, 0, 100, and 200 V, which are displayed in figure 5.6. This data also demonstrates the measured density variation with strain through the shifting of the SdH minima. However, there is a discrepancy between the zero-field intercepts of the R_{yy} magnetotransport in figure 5.6 and the zero-field directional resistance measurements in figure 5.3 for positive piezo bias voltage. In the magnetotransport tests, zero-field R_{yy} rose and then fell again as the piezo bias voltage changed from zero to 100 and to 200 V, in contrast to the large monotonic rise illustrated in figure 5.3. We do not have an explanation for this disagreement, other than to note that the sample was altered by the application of strain, as shown in figure 5.1, between the two series of tests.

5.4 Discussion

Through PH-9, we successfully measured the effects of uniaxial strain application along [110] on a 2DES. The effects of strain appear perturbative on the 2DES sample characteristics. Uniaxial strain changed the sample density with a slope $\left(\frac{\Delta N_s / N_s}{\epsilon_x}\right) \simeq -1.47 \times 10^3$. We do not have an explanation for this effect, though we hypothesize that it could arise from strain-induced changes in the band-gap alignment of the heterostructure.

We can compare our density result in order of magnitude with the density effects of hydrostatic pressure by converting the principle uniaxial strain into an approximate hydrostatic pressure through treating it as an isotropic strain:

$$\left(\frac{\Delta P}{B}\right) = \left(\frac{\Delta V}{V}\right) = 3\ \epsilon_{isotropic} \sim 3\ \epsilon_x$$

For GaAs, the bulk modulus is $B \sim 10^{12}$ dynes/cm^2. We applied strain of about 3×10^{-5}, which converts into an effective pressure $P \sim 10^8$ dynes/cm^2 = 0.1 kbar. Therefore we observed a normalized density change of 0.1/0.1kbar from uniaxial strain application. W. Kang [14] measured a normalized density change of order 0.1/kbar for hydrostatic pressure application in a similar 2DES sample. In comparison, our effect is about an order larger. Unfortunately, the effect of uniaxial strain on the g-factor is hard to determine from our data, apart from the observation that any such effect is small for our strain size, and so we cannot make a comparison about the g-factor with hydrostatic pressure tests.

Surprisingly, uniaxial strain caused the zero-field directional resistance to change in a non-uniform manner, with R_{yy} a complicated function of the applied strain. We cannot explain this detail or the observed discrepancy between the two sets of zero-field R_{yy} data for positive piezo bias voltage. We

are also unsure of why the sample changed density during measurement. We are concerned that we did not fully repair the ground-shield on PH-9, as the metal layer was broken underneath the sample where we cannot analyze it. Thus, we are unsure whether or not the ground-shield covers the entire underside of the 2DES. To address the ground-shield concerns and PH-9 data discrepancies, we plan to investigate further with the next PH in development, PH-11, which will utilize an improved ground-shield once completed.

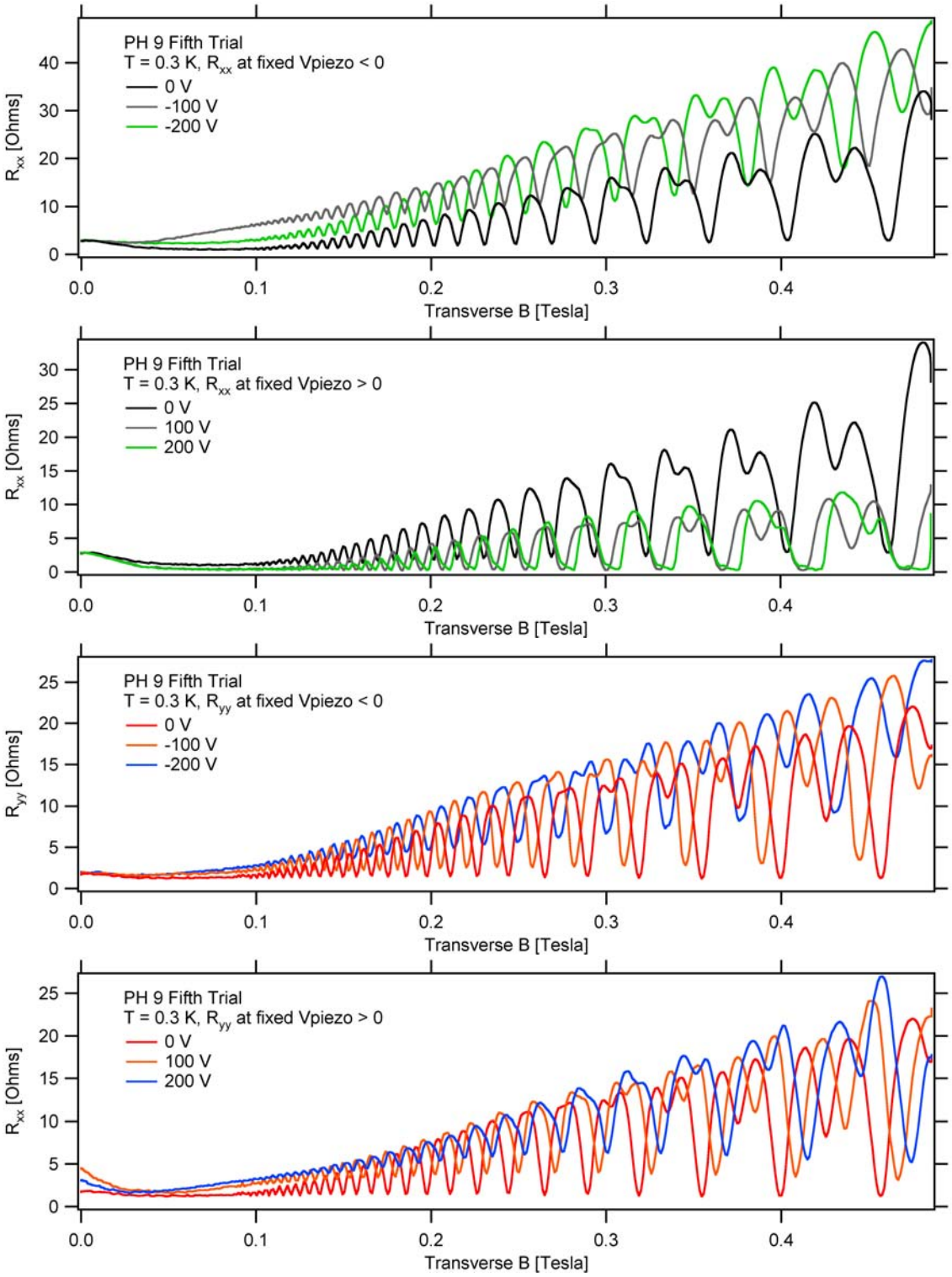

Figure 5.6: *PH-9 fifth trial, with repaired ground-shield and open-lead cool-down. SdH minima shift in conjunction with the strain-induced density change. A shift right or left corresponds to an increase or decrease respectively in density. The top two graphs correspond to R_{xx}, and the bottom two to R_{yy}. Results are divided for positive and negative piezo-bias.*

Chapter 6

Conclusion

The goal of this project was to perfect a method of applying controllable uniaxial strain on two-dimensional electron systems at cryogenic temperatures and in the presence of large magnetic field strengths, with the ultimate aim of utilizing this technique to investigate the alignment mechanism of the anisotropic stripe state. In retrospect, we recognize that the project motivation was very ambitious. However, we have successfully developed a difficult method for the cryogenic application of uniaxial strain, and we have initially measured the effects of uniaxial strain on 2DESs.

We have demonstrated that our current piezo-header approach works down to T = 0.3 K and in the presence of magnetic fields strengths of up to 0.63 Tesla, and that we can successfully apply strains of up to about $\pm 5 \times 10^{-5}$ on 2DES samples. We are unaware of any limitations that would prevent the extension of our technique to lower temperatures and higher magnetic field strengths, which are necessary for the study of the stripe state. Through PH-9, we have shown that our current design can be used to study the effects of uniaxial strain on samples.

Moreover, we have measured the effects of uniaxial strain applied principally along the [110] crystallographic axis on a 2DES, demonstrating that strain alters the sample characteristics, most notably density, in a perturbative manner. Work is under way to verify our results with a new piezo-header, PH-11, which will use a sample with a good stripe state. If the construction and tests of PH-11 are successful, we will push PH-11 into the more restrictive environment needed to study the stripe state. With luck, we may get to apply our method to study the stripe state orientation mechanism in the near future.

Appendix A

Strain

A.1 Introduction

Strain is a measure of length deformation. The two standard definitions for strain are listed below, where l is a length with a nominal value of l_0 [17]:

Engineering Strain e is the fractional change of length:

$$e \equiv \frac{l - l_0}{l_0} = \frac{\Delta l}{l_0}$$

True Strain ϵ is the integral of all instantaneous length changes:

$$\epsilon \equiv \int_{l_0}^{l} \frac{dl}{l_0} = \ln\left(\frac{l}{l_0}\right) = \ln(1+e)$$

For small strain, both definitions are equivalent to first order in the expansion of the true strain, $\epsilon = ln(1+e) = e + \frac{1}{2}e^2 + \ldots \approx e$.

Of the two, engineering strain is the more common form. True strain, however, is the only definition that remains additive for large strain, where engineering strain breaks down. Engineering strain is particularly convenient in that rearranging its definition yields a particularly useful substitution for the length l, which also holds for small true strain:

$$l = l_0(1+e) \tag{A.1}$$

The strains encountered in this project are on or below the order of 10^{-4}. For this reason, strain has been denoted using the symbol for true strain, ϵ, even though the strain measurements performed actually measure engineering strain.

A.2 Uniaxial Strain

The most important type of strain to this project is uniaxial strain:

Uniaxial Strain is directional strain applied along one cartesian axis.

While there are other types of strain, such as shear and bending, the use of the term "strain" in this document is meant to refer to uniaxial strain unless otherwise noted.

A.3 Solid Deformation and Poisson Strain

For small strain, we can use (A.1) to rewrite the volume of a solid:

$$\frac{V}{V_0} = (1+\epsilon_x)(1+\epsilon_y)(1+\epsilon_z) \approx 1+\epsilon_x+\epsilon_y+\epsilon_z$$

For an ideally incompressible solid, uniaxial strains applied on all three cartesian axes are not independent due to volume conservation. Instead, they must sum to zero:

$$\Delta V = 0 \rightarrow \epsilon_x+\epsilon_y+\epsilon_z = 0 \tag{A.2}$$

This relation between orthogonal uniaxial strains implies that applying uniaxial strain along one direction also renders uniaxial strain along the transverse directions. In fact, the resultant strains are called Poisson strain:

Poisson Strain is uniaxial strain induced in a material transverse to an applied uniaxial strain.

Poisson's Ratio n is the negative ratio of an applied strain and its Poisson strain.

For example, applying ϵ_x on a ideally incompressible ($\Delta V = 0$) solid will result in $\epsilon_y = \epsilon_z = -\left(\frac{1}{2}\right)\epsilon_x$, where the Poisson ratio is equal to $-\left(\frac{\epsilon_x}{\epsilon_y}\right) = -\left(\frac{\epsilon_x}{\epsilon_z}\right) = 2$. This value of $n = 2$ for the Poisson ratio is the most typical value, though in reality, most solids are not ideally incompressible, and so Poisson's ratio depends on the material in question. Interestingly, there are even some structures with negative Poisson's ratio [18].

Poisson's ratio can vary with the direction of strain application, due to the materials structure or external constraints. For example, if we apply strain along the x direction in a solid while some load is placed upon the y direction, then the Poisson's ratio for Poisson strain in the y and z direction may differ. In this case, the Poisson's ratio in the y direction would be greater than that in the z direction, reflecting that Poisson strain was greater in the z direction than in the y direction.

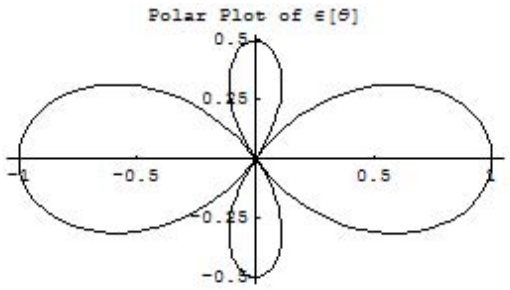

Figure A.1: *Normalized polar plot of $\epsilon(\theta)$ for a material with a Poisson's ratio of 2, as given by equation A.5.*

A.4 Directional Strain in Two-Dimensions

Applying dissimilar small uniaxial strains ($\epsilon_x \neq \epsilon_y$) in two-dimensions creates a $cos(2\theta)$ distortion in the directional strain $\epsilon(\theta)$ about any point in the sheet, where θ is measured off of the x axis:

$$\epsilon(\theta) = \left(\frac{\epsilon_x + \epsilon_y}{2}\right) + \left(\frac{\epsilon_x - \epsilon_y}{2}\right)\cos(2\theta) \tag{A.3}$$

As a consequence, applying dissimilar uniaxial strain in two-dimensions on a lattice will create a superposition of a uniform strain and a $cos(2\theta)$ distortion in the lattice.

Note that in practice only one uniaxial strain needs to be applied to generate a $\cos(2\theta)$ distortion, as Poisson strain will normally provide the other dissimilar uniaxial strain. We can rewrite equation A.3 to reflect this by incorporating the Poisson ratio $n = -\left(\frac{\epsilon_y}{\epsilon_x}\right)$:

$$\epsilon(\theta) = \frac{\epsilon_x}{2}\left[(1 - \frac{1}{n}) + (1 + \frac{1}{n})\cos(2\theta)\right] \tag{A.4}$$

For a material with a Poisson's ratio of 2, this directional strain evaluates to the following, as displayed in figure A.1:

$$\epsilon(\theta) = \frac{\epsilon_x}{4}\left[1 + 3\cos(2\theta)\right] \tag{A.5}$$

In truth, equation A.3 is an approximation valid for small strain, which can be derived in the following manner. Consider the right triangle in figure A.2. $\epsilon(\theta)$ is the appropriate uniaxial strain

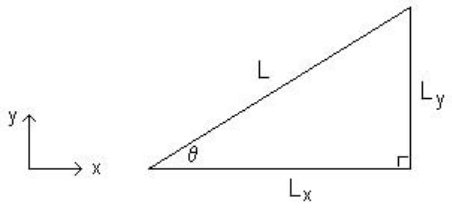

Figure A.2: *Geometric setup for directional strain derivation.*

along the hypotenuse of this triangle. Using the pythagorean theorem and equation A.1, we can write:

$$L^2 = L_x^2 + L_y^2 \rightarrow L^2(1+\epsilon(\theta))^2 = L_x^2(1+\epsilon_x)^2 + L_y^2(1+\epsilon_y)^2$$

Dropping the quadratic terms, we get the following small strain approximation:

$$L^2(1+2\epsilon(\theta)) \approx L_x^2(1+2\epsilon_x) + L_y^2(1+2\epsilon_y)$$

After subtracting L^2 from both sides, we can rewrite this in the following manner:

$$\begin{aligned}
\epsilon(\theta) &\approx \left(\frac{L_x}{L}\right)^2 \epsilon_x + \left(\frac{L_y}{L}\right)^2 \epsilon_y \\
&\approx cos^2(\theta)\epsilon_x + sin^2(\theta)\epsilon_y \\
&= \frac{1}{2}(1+cos(2\theta))\epsilon_x + \frac{1}{2}(1-cos(2\theta))\epsilon_y \\
&= \left(\frac{\epsilon_x+\epsilon_y}{2}\right) + \left(\frac{\epsilon_x-\epsilon_y}{2}\right)\cos(2\theta)
\end{aligned}$$

This is equation A.3, the desired result.

A.5 Strain Distribution in 2DES Samples

Piezo-headers apply dissimilar strain in the two-dimensions in-plane with the 2DES due to the Poisson ratio and loading of the actuator, as discussed in the previous section. Both in-plane strains, ϵ_x and ϵ_y, are measurable using strain gauges affixed to the opposite side of the piezo-actuator [1]. Therefore, the amount of $\cos(2\theta)$ distortion generated by uniaxial strain is calculable from strain gauge measurements using equation A.3. Under the assumption of volume conservation, we may also estimate the amount of strain generated through the thickness of the sample, ϵ_z, using equation A.2.

Appendix B

Strain Measurement

B.1 Strain Gauges

Metal-foil strain gauges are a common device used to measure strain, consisting of a thin metal film pattern arranged such that the resistance of the pattern varies in response to uniaxial strain along one measurement axis. These devices are attached to a material such that any deformation of the material also deforms the gauge. Figure B.1 is a picture of one type of strain gauge used in this project.

Strain gauges vary their resistance in response to applied directional strain in the following way, where R^o_{sg} is the nominal gauge resistance and GF is a "gauge factor" determined by the manufacturer (typically ≈ 2):

$$R_{sg} = R^o_{sg}(1 + GF \cdot \epsilon) \tag{B.1}$$

Therefore strain gauges turn the problem of measuring strain into the problem of measuring small changes in a resistance. Luckily, there is a very convenient circuit that can measure changes in electrical resistance, the Wheatstone bridge.

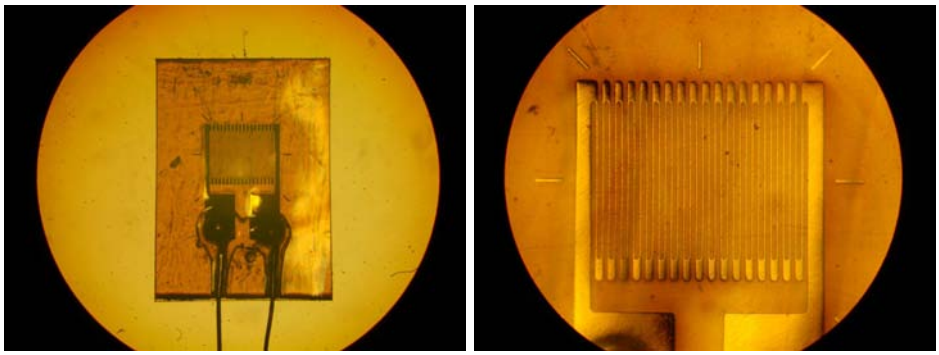

Figure B.1: *Optical microscope enlargements of an Omega SG-2/350-LY11 strain gauge pattern. The picture to the right is a close up of the gauge pattern.*

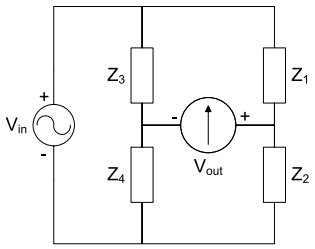

Figure B.2: *Basic Wheastone bridge circuit diagram.*

B.2 Wheatstone Bridge

The Wheatstone bridge is a very useful instrument for measuring the value of an unknown component or measuring small changes in component values. Figure B.2 is an example Wheatstone bridge circuit diagram featuring four impedances, Z_1 to Z_4, an ideal voltage source, and an ideal voltmeter. The output of the Bridge is given by the difference of the outputs of the two voltage divider "legs" of the circuit:

$$\frac{V_{out}}{V_{in}} = \left(\frac{Z_2}{Z_1 + Z_2}\right) - \left(\frac{Z_4}{Z_3 + Z_4}\right) \tag{B.2}$$

In practice, the impedances can be either resistors, capacitors, or inductors. However, both components on a leg must be of the same type to function as a voltage divider. The two legs need not be composed of the same type of components.

By careful adjustment of the impedances, the output of the Bridge can be set to zero, or "nulled." When this is the case, we have the following condition, where N_0 is taken to be the voltage dividing ratio of the two legs of the bridge when nulled:

$$N_o = \left(\frac{Z_2}{Z_1 + Z_2}\right) = \left(\frac{Z_4}{Z_3 + Z_4}\right) \tag{B.3}$$

In essence, nulling makes Wheatstone bridges useful. For example, a Wheatstone bridge can be used to determine an unknown component value through the process of nulling. The typical procedure is the following: Put the component in question on one leg of the bridge, together with a calibrated component of the same type. Replace the other leg of the bridge with an adjustable voltage divider, and use this divider to null the bridge. Measure the ratio of the adjustable voltage divider, and then use the nulling condition (equation B.3) to solve for the unknown component value.

A Wheatstone bridge can also be used to measure small changes in its components after nulling. Let us examine what happens if we allow two impedances on one leg of the Bridge to deviate slightly in value. For δ_1 and δ_2 small, take:

$$\begin{cases} Z_1 \to Z_1(1 + \delta_1) \\ Z_2 \to Z_2(1 + \delta_2) \end{cases}$$

Incorporating these changes and neglecting quadratic and higher order terms in the deviations, we can make the following approximation:

$$\begin{aligned}\left(\frac{Z_2}{Z_1+Z_2}\right) &\rightarrow \left(\frac{Z_2(1+\delta_2)}{Z_1(1+\delta_1)+Z_2(1+\delta_2)}\right)\\ &= \left(\frac{Z_2(1+\delta_2)}{Z_1+Z_2+Z_1\delta_1+Z_2\delta_2}\right)\\ &= N_o(1+\delta_2)\left[\frac{1}{1+(1-N_o)\delta_1+N_o\delta_2}\right]\\ &\approx N_o(1+\delta_2)\left[1-(1-N_o)\delta_1-N_o\delta_2\right]\\ &\approx N_o\left[1-(1-N_o)\delta_1+(1-N_o)\delta_2\right]\\ &= N_o+N_o(1-N_o)(-\delta_1+\delta_2)\end{aligned}$$

Using this result, we can now evaluate the Bridge response to the component value deviations:

$$\frac{V_{out}}{V_{in}} \approx N_o(1-N_o)(-\delta_1+\delta_2) \tag{B.4}$$

This equation is known as the half-bridge equation, since only the components of one leg of the bridge were permitted to change. If we allow the other two impedances to vary, by introducing δ_3 and δ_4, then we get the following more general result:

$$\frac{V_{out}}{V_{in}} \approx N_o(1-N_o)(-\delta_1+\delta_2+\delta_3-\delta_4) \tag{B.5}$$

This equation is known as the full-bridge equation, since it incorporates the deviations of all four bridge components.

Examining the half and full-bridge equations, we see that a nulled bridge deviates from zero proportionally with small changes of its component values. However, please take note of the signs, which for example serve to cancel any common deviation between two components on the same leg. These general results form the basis for the measurement of strain using strain gauges in this project.

B.2.1 Wheatstone Bridge with Strain Gauges

There are many configurations for incorporating strain gauges into a Wheatstone bridge, due not only to the number and placement of strain gauges into the circuit, but also the combinations of possible orientations of the strain gauges with respect to the strains to be measured. The simplest arrangement consists of placing a single strain gauge into a Wheatstone bridge. For example, consider replacing Z_1 in figure B.2 with a strain gauge. Using equations B.1 and B.4, the output of the bridge

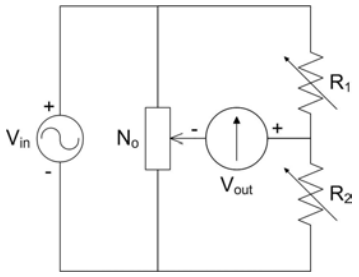

Figure B.3: *Simplified half-bridge strain measurement circuit using two strain gauges, R_1 and R_2. This is the basic configuration of the strain measurement circuit used in this project.*

will be the following:

$$\frac{V_{out}}{V_{in}} = -\left[N_o(1-N_o)GF\right]\epsilon$$

Thus, after nulling, this configuration yields an output proportional to the applied strain.

However, other factors, such as temperature and magnetic field fluctuation, affect the resistance of a strain gauge. The single strain gauge bridge is unable to differentiate between the effects of strain and the effects of these other factors. Therefore, a single strain gauge bridge requires extra caution to minimize these external effects in oder to accurately measure strain.

These external effects can be canceled by incorporating two strain gauges into one leg of the bridge, such as in figure B.3. Physically arranging the two strain gauges, R_1 and R_2, such that they share the same external influences ensures that these effects are canceled out. We can see explicitly by making the following substitution into the half-bridge equation:

$$\begin{cases} \delta_1 \rightarrow GF \cdot \epsilon_1 + \delta_{error} \\ \delta_2 \rightarrow GF \cdot \epsilon_2 + \delta_{error} \end{cases}$$

After substitution into equation B.4, the bridge output becomes:

$$\frac{V_{out}}{V_{in}} = N_o(1-N_o)GF(-\epsilon_1 + \epsilon_2)$$

Typically, when two gauges are used in this sort of configuration, only one is active. The other one is used only to cancel out any common signal. Taking R_1 as the active strain gauge, and R_2 as the passive strain gauge, the bridge output is now:

$$\frac{V_{out}}{V_{in}} = -\left[N_o(1-N_o)GF\right]\epsilon_1 \tag{B.6}$$

Usually $N_o \approx 1/2$ and $GF \approx 2$, so the pre-factor is typically -($1/2$). We used this temperature compensated half-bridge arrangement for our strain measurements with great success. Many other configurations are possible, and are commonly used in strain measurement elsewhere.

Appendix C

Piezo-Header Addendum

C.1 Parts

We used the same style of low-voltage piezo-mechanical stack actuators from Piezomechanik GmbH as used by [1]: PSt 150/5x5/7. However, we primarily use the cryogenic version of these actuators, PSt 150/5x5/7 TT, not mentioned in [1], as we found the standard version cracks from cooling. The cryogenic version is very reliable, and does not failed through normal piezo-header usage.

We used two types of inexpensive strain gauges from Omega Engineering, Inc: SG-2/350-LY11 and SG-3/350-XY11. Both have a base resistance of 350 Ω and a gauge factor of about 2 (calibrated numbers are provided by the manufacturer). The LY11 model was one of two types used in [1]. The LY11 model features a single gauge, while the XY11 gauges feature two overlapping orthogonal gauges. The earliest piezo-headers used the LY11 gauges for strain measurement, and the latest models use the XY11 gauges for strain measurement, along with a passive LY11 gauge for temperature compensation.

We use Emerson & Cuming Stycast 1266, a two component, low viscosity clear encapsulant, for strain gauge and sample attachment to the piezo-header. We investigated the use of UHU Plus Endfest 300, as used in [1], but found Stycast 1266 to be better suited for our approach. We also investigated the use of Miller-Stephenson MS-111, a powerful stripping agent, to dissolve Stycast 1266 and remove attached samples. While we did not try this solvent on an actual piezo-header, other test results suggest that MS-111 could be used to remove samples.

We used EPO-TEK H2OE conductive silver epoxy for connections to the evaporated ground shield.

C.2 Detailed Construction

Here are the steps involved in constructing a piezo-header:

1. Attach Strain Gauges to Piezo-Actuator

- Flatten solder joints on strain gauge using a Hoffman clamp and heating to 80° C for 5 minutes. Re-clamp and repeat.
- Prepare the Hoffman clamp with a layer of teflon over the clamp faces.
- Prepare strain gauge and piezo-actuator for attachment. Visually inspect the strain gauge, and double check its base resistance with a multimeter. Cut down the strain gauge polyimide backing as necessary with a razor blade. Double check gauge orientation such that the x-gauge is closest to the piezo-actuator, and the solder joints point away from the piezo-actuator.
- Mix and vacuum impregnate Stycast 1266 epoxy.
- Place a small drop of epoxy on the piezo-actuator.
- Affix and align the strain gauge.
- Wrap the piezo-actuator and strain gauge tightly with teflon tape to hold the alignment.
- Double check strain gauge alignment through the teflon tape, and nudge to correct if necessary.
- Clamp the piezo-actuator and strain gauge assembly in the Hoffman clamp, to flatten the strain gauge to the piezo-actuator.
- Vacuum impregnate for about 5-10 minutes.
- Cure at 80-90° C for 1-2 hours.
- Remove all teflon and clean the piezo-actuator top surface with isopropanol, if necessary.

2. Assemble the Piezo-Header Body

   - Prepare an 18 pin electrical header. Cut down top pin heights as necessary.
   - Attach the wires from piezo-actuator and strain gauge assembly to the electrical header.
   - Attach a passive free strain gauge to the header. Cut down the strain gauge backing with a razor blade to reduce its size.
   - Double check the wiring. Ensure strain gauge wires do not touch.
   - Clean the top face of the piezo-actuator with isopropanol.

3. Ground Shield (in the manner of PH-8 to PH-10)

   - Clean the piezo-actuator top surface.
   - Evaporate a 2000 Å thick aluminum layer onto the top surface.
   - Attach a wire to the metal layer with conductive epoxy, and connect it to the header.

4. Attach Sample to Piezo-Header Body

   - Process Sample
   - Temporarily wire-up sample to a header, and characterize it at T = 0.3 K.
   - Replace the wires to the sample with longer ones for the PH.
   - Carefully clean the sample underside, if possible, to remove any debris such as indium bits.
   - Clean the piezo-actuator top surface.
   - Use a small drop of epoxy to attach the sample.
   - Push gently with thinned wooden applicator sticks on the sample.
   - Finish sample alignment, and then cure at 80-90° C for 1-2 hours.
   - Wire up the sample to the header.

5. Finishing Steps

   - Tie down the piezo-actuator to the body with dental floss.
   - Double check the wiring layout for shorts.
   - Build a safe contained to store the piezo-header.

Appendix D

Sample Processing

D.1 Cleaving

Figure D.1 is a graphic depiction of the typical cleaving, contacting, and wire-up process for an unprocessed sample. If needed, processing is performed immediately after cleaving and before contacting.

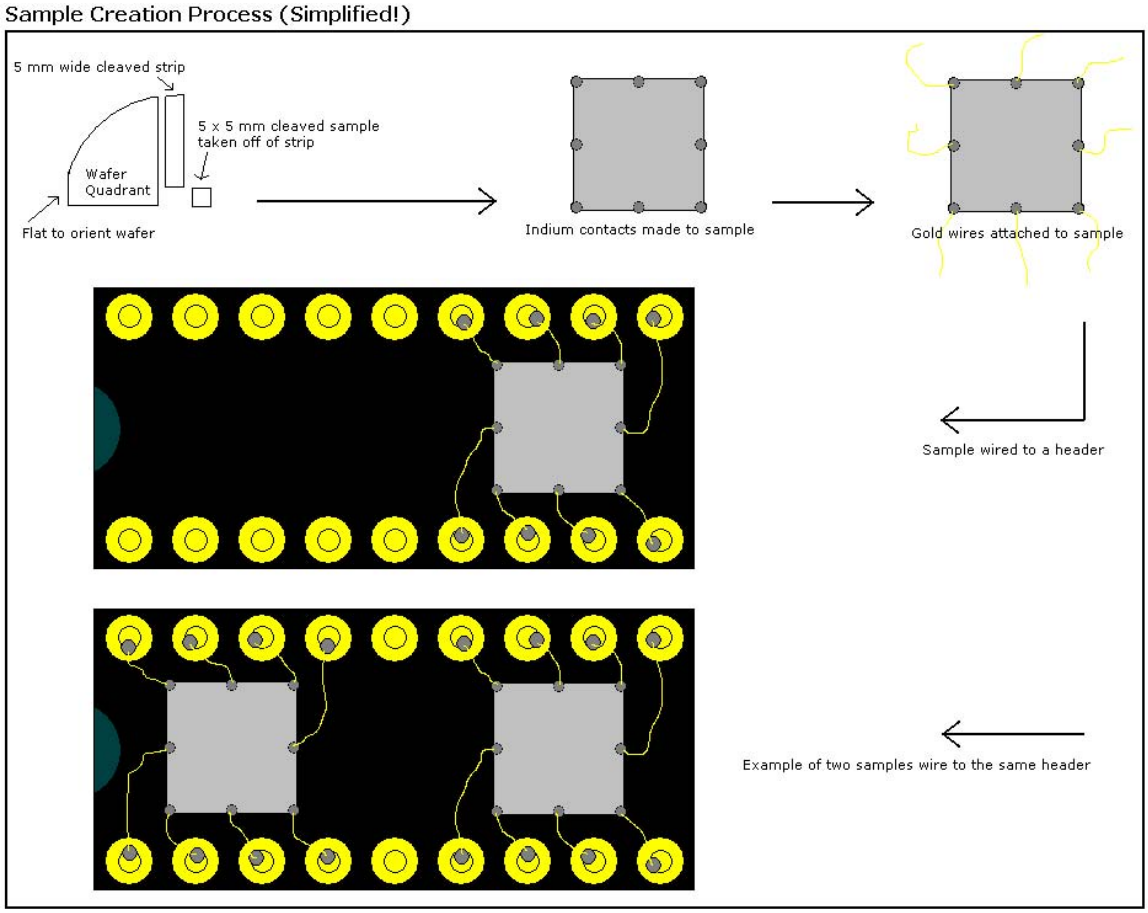

Figure D.1: *Illustration of sample cleaving and wire-up.*

D.2 Thinning

Thinning may be performed before or after photolithography. Thinning after photolithography, however, simplifies the processing steps. Here is a typical thinning procedure:

- Clean quartz disc with acetone at 60° C for 3 minutes, rinse with isopropanol.
- Mount cleaned sample(s) with wax onto disc.
- Measure sample thickness.
- Find scrap samples of the same thickness.
- Clean and mount the dummies to balance load during thinning.
- Remove excessive mounting wax with warm acetone for 10 minutes, followed by isopropanol rinse.
- Setup quartz plate with filter paper cover in a tub.
- Mix ∼10% etching solution, ex: 35 mL Methanol, 5.2 mL Bromine.
- Etch using steady figure-eight strokes upon the filter paper wet with etching solution. Pause to measure thickness. Repeat until desired thickness is reached.
- Remove dummies with razor blade.
- Remove sample with acetone at 60° C for ∼ 1 hour.
- Clean sample with IPA and dry.

D.3 Photolithography

Photolithography is used to mesa-etch and lay contacts upon the 2DES. The following subsections describe the different procedures used during photolithography.

D.3.1 Sample Cleaning

Here is the typical procedure to clean a cleaved sample before photolithography:

- Boil in trichloroethylene at 150° C for 15 minutes
- Sonicate in acetone for 5 minutes
- Sonicate in isopropanol for 3 minutes

D.3.2 Mesa-Etch

The following is the typical mesa-etch procedure:

- Clean sample.
- If necessary, clean photo-masks in acetone, rinse in IPA.
- Spin AZ5214E photomask onto sample at 5,000 rpm for 30 seconds.
- Bake at 100° C for 45 seconds.
- Expose pattern with UV for 40 seconds.
- Develop using AZ400K 1:4 solution for 2 minutes.
- Post-bake at 120° C for 70 seconds

- Mix phosphoric acid solution: 100 mL H_2O, 10 mL H_3PO_4, 2 mL H_2O_2.
- Stir with bar magnet.
- Etch for 5 minutes.
- Rinse in deionized water (DI).
- Measure the height of the mesa.
- Remove resist in n-butyl acetate at 75° C for 15 minutes.
- Rinse in IPA.

D.3.3 Ohmic Contacts Mask

Metal contacts are evaporated onto mesa-etched samples using a contacts mask. Metal is evaporated onto the sample, and the mask is removed, leaving metal behind only inside the desired contacts pattern. The following list is a typical procedure to create a contacts mask:

- Sonicate sample in acetone for 5 minutes.
- Sonicate sample in IPA for 3 minutes.
- Spin AZ5214E photomask onto sample at 5,000 rpm for 30 seconds.
- Bake at 100° C for 45 seconds.
- Expose pattern with UV for 40 seconds.
- Develop using AZ400K 1:4 solution for 50 seconds.
- Rinse in DI.

D.3.4 Evaporating Ohmic Contacts

The following list is a typical procedure for evaporating ohmic contacts onto a sample with a contacts mask. We typically shoot for contacts deposition of 135 Å Ni and 1500 Å AuGe.

- Attach sample onto a glass slide face-up with rubber cement.
- Load sample and contacts metals into evaporator.
- Pump down the bell jar.
- Perform a dummy evaporation, if desired, to purify the contacts metals. Pump down again following a dummy evaporation.
- Evaporate the contacts.
- Remove sample from the evaporator.
- Liftoff the contacts mask in n-butyl acetate at 60° C.
- Rinse in IPA.
- Sonicate in acetone, and then IPA as before.
- Take a picture.
- Anneal at 445° C for 10 minutes in a forming gas environment.
- Take a picture.

Appendix E

About This Document

This document was written with pdfLaTeX and BibTeX using TeXShop. The style was adapted from a Caltech thesis class from Daniel M. Zimmerman, available online at http://www.cs.caltech.edu/~dmz/thesis-class/.

Bibliography

[1] M. Shayegan, K. Karrai, Y. Shkolnikov, K. Vakili, E. D. Poortere, and S. Manus, Appl. Phys. Lett. **83**, 5235 (2003).

[2] J. H. Davies, *The Physics of Low-Dimensional Semiconductors: An Introduction* (Cambridge University Press, New York, NY, 1998).

[3] S. M. Girvin, The Quantum Hall Effect: Novel Excitations and Broken Symmetries, 2000.

[4] M. Lilly, K. Cooper, J. Eisenstein, L. Pfeiffer, and K. West, Phys. Rev. Lett. **82**, 394 (1999).

[5] K. Cooper, M. Lilly, J. Eisenstein, T. Jungwirth, L. Pfeiffer, and K. West, Solid State Commun. **119**, 89 (2001).

[6] K. B. Cooper, Ph.D. thesis, California Institute of Technology, 2003.

[7] E. Fradkin, S. A. Kivelson, E. Manousakis, and K. Nho, Phys. Rev. Lett. **84**, 1982 (2000).

[8] J. Eisenstein, Solid State Commun. **117**, 123 (2001).

[9] M. Lilly, K. Cooper, J. Eisenstein, L. Pfeiffer, and K. West, Phys. Rev. Lett. **83**, 824 (1999).

[10] L. Tracy, J. Eisenstein, M. Lilly, L. Pfeiffer, and K. West, Solid State Commun. **137**, 150 (2005).

[11] J. Zhu, W. Pan, H. Stormer, L. Pfeiffer, and K. West, Phys. Rev. Lett. **88**, 116803 (2002).

[12] J. Mercy, C. Bousquet, J. Robert, A. Raymond, G. Gregoris, J. Beerens, J. Portal, P. Frijlink, P. Delescluse, J. Chevrier, and N. Linh, Surface Science **142**, 298 (1984).

[13] D. Maude, M. Potemski, J. Portal, M. Henini, L. Eaves, G. Hill, and M. Pate, Phys. Rev. Lett. **77**, 4606 (1996).

[14] W. Kang, J. Young, S. Hannahs, E. Palm, K. Campman, and A. Gossard, Phys. Rev. B **56**, 12776 (1997).

[15] L. van der Pauw, Phillips Res. Repts. **13**, 1 (1958).

[16] L. van der Pauw, Phillips Tech. Rev. **20**, 220 (1958).

[17] C. R. Barrett, W. D. Nix, and A. Tetelman, *The Principles of Engineering Materials* (Prentice-Hall, Engelwood Cliffs, NJ, 1973).

[18] R. Lakes, Science **235**, 1038 (1987).